TÉCNICO LISBOA

Wavelength Multiplexer

Gonçalo Alves Cavaco

Thesis to obtain the Master of Science Degree in

Electrical and Computing Engineering

Supervisors : Professor João Paulo Neto Torres
Professor António Carlos De Campos Simões Baptista

Examination Committee

Chairperson: Professor Teresa Maria Canavarro Menéres Mendes de Almeida
Supervisor: Professor António Carlos De Campos Simões Baptista
Member of the Committee: Professor Maria João Marques Martins

November 2023

I declare that this document is an original work of my own authorship and that it fulfils all the requirements of the Code of Conduct and Good Practices of the *Universidade de Lisboa*.

Resumo

A Multiplexação por divisão no comprimento de onda é uma tecnologia desenvolvida para aplicações em telecomunicações com o objetivo de combinar inúmeros sinais de comprimento de onda num único canal. Os multiplexadores podem ser usados como componentes passivos ou ativos de redes em telecomunicações. Estes componentes, geridos por mecanismos externos, podem ser filtros, lasers ou amplificadores.

O objetivo desta pesquisa é a caracterização de ressoadores em anel com guias de onda planares. A resposta na saída desses sistemas é analisada, para diferentes configurações, dimensões e materiais, através da variação de um conjunto de parâmetros, utilizando o método dos elementos finitos implementado no *COMSOL.*

A representação da luz como uma onda eletromagnética e as suas características de propagação através de uma estrutura confinada, como um guia de onda planar, estão definidas. Além disso, os ressoadores em anel são analisados e descritos por métodos analíticos e numericamente pelo método dos elementos finitos.

Os resultados de transmitância de saída demonstram que a mudança de dimensões e materiais do núcleo para as configurações analisadas dos ressoadores de anel permitem o ajuste do número de comprimentos de onda na ressonância, da largura de ressonância, e da transmitância fora da ressonância. Os ressoadores em anel podem funcionar como multiplexadores de comprimento de onda, com a transmissão dos comprimentos de onda de ressonância.

Palavras-chave

Multiplexador, guias de onda óticos, ressoador em anel, método dos elementos finitos, método analítico.

Abstract

The Wavelength Division Multiplexing, WDM, is a technology developed for applications in telecommunications with the purpose of combining numerous wavelengths signals into one single channel. The multiplexers can be used as passive or active components of telecommunications networks. These components managed by external mechanisms, can be filters, lasers, or amplifiers.

The aim of this research is the characterization of ring resonators with planar optical waveguides. The output response of these systems is analysed for different configurations, dimensions, and materials, by varying a set of parameters using the finite element method, FEM, implemented in *COMSOL*.

The representation of the light as an electromagnetic wave and its propagation features across a confined structure, such as a planar optical waveguide, are defined. Besides, the ring resonators, RR, are analysed and described by the analytical methods, and numerically by the finite element method.

The results of the output responses demonstrate that the change of dimensions and core materials for the analysed configurations of the ring resonators allow the adjustments of the resonance wavelength number, of the resonance width, and of the transmittance outside resonance. Furthermore, the ring resonators can work as wavelength multiplexers, with the transmission of the resonance wavelengths.

Keywords

Multiplexer, optical waveguides, ring resonator, finite element method, analytical method.

Contents

List of Figures

List of Tables

Acronyms

FEM	Finite Element Method
FSR	Free Spectral Range
FWHM	Full Width at Half Maximum
LASER	Light Amplification by Stimulated Emission of Radiation
PDE	Partial Differential Equations
RR	Ring Resonator
TE	Transversal Electric
TM	Transversal Magnetic
WDM	Wavelength Division Multiplexing

Nomenclature

A_i, B_i	Coupling coefficients of coupler *i*
c_0	Speed of light in vacuum
d	Distance between waveguides
$\boldsymbol{E}$	Electric field vector
$\bar{\boldsymbol{E}}$	Complex vector of the electric field
f	Linear frequency
f_0	Reference frequency
F	Finesse
$\boldsymbol{H}$	Magnetic field vector
$\bar{\boldsymbol{H}}$	Complex vector of the magnetic field
n	Refractive index
n_{clad}	Cladding refractive index
n_{core}	Core refractive index
n_{eff}	Effective refractive index
n_g	Group refractive index
n_{sub}	Substrate refractive index
ℓ	Coupling length
L	Perimeter of the ring-shaped waveguide
r	Radius of the ring-shaped waveguide
k	Wavenumber of the light
Q	Quality factor
T	Transmittance factor
T_{max}	Maximum Transmittance
T_{min}	Minimum Transmittance
T_p	Transmittance of port *p*
w	Thickness of the waveguides

β	Propagation constant
γ_i	Intensity loss coefficient of coupler i
Δ	Relative refractive index
δ	Half the difference between two propagation constants
ε_0	Electric permittivity in vacuum
η	Maximum power coupling efficiency
θ	Incident angle of the light
θ_{max}	Maximum incident angle of the light
κ	Real coupling coefficient
λ	Wavelength
λ_{res}	Resonance wavelength
λ_0	Wavelength of the light in vacuum
μ_0	Magnetic permeability in vacuum
ρ	Amplitude attenuation coefficient
τ	Amplitude transmission factor
ϕ	Inclination angle or optical phase
ϕ_0	Additional phase shift
ω	Angular frequency

1

Introduction

1.1 Basic aspects of optical wavelength multiplexing systems

The Wavelength Division Multiplexing, or WDM, technology concept goes back to the year of 1970 [1,2]. Since then, this technology has been a subject of research and development regarding telecommunications, whether in optical fibers, planar waveguides, or even free space transmission. Nowadays, WDM technology plays a significant role in optical communications networks around the planet, in a world with a constant need of faster transmission rates allied to increased bandwidth.

WDM allows the combination of several independent wavelength signals into one single optical channel. This concept is the basis of the wavelength multiplexers, which are only a part of WDM networks, as seen in Figure 1.1. These networks have also other components such as light sources composed by lasers, optical amplifiers, and receivers with optical filters, which can be passive or active devices. An active device has an external control mechanism to monitor and assure a successful functionalization.

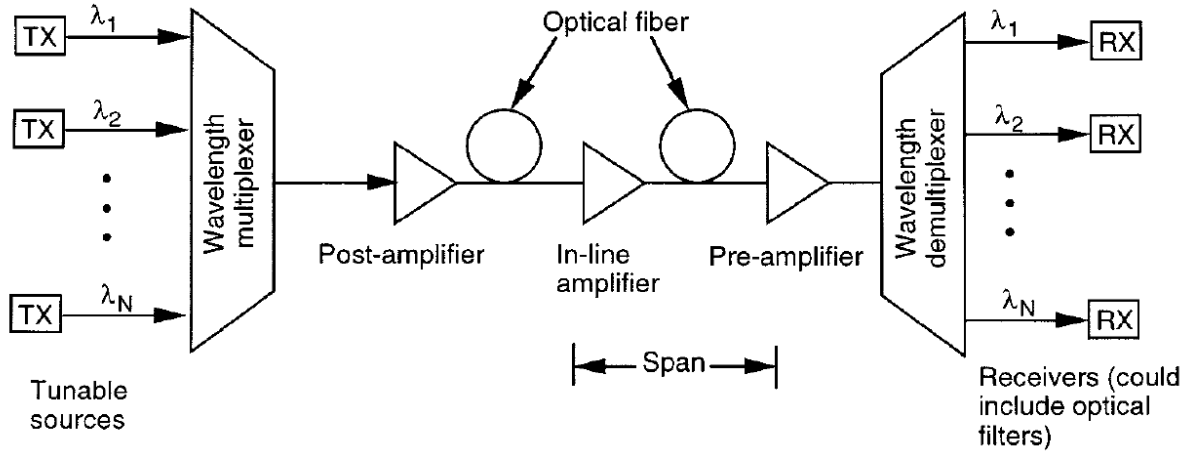

Figure 1.1 – Typical implementation of a WDM link (from [3]).

A wavelength multiplexer can be fabricated with planar optical waveguides or optical fibers. These wavelength multiplexers, which have couplers of distinct types of waveguides can be array waveguide grating multiplexers or can be based on fiber grating if assembled with fibers, [4,5]. Despite the materials that are part of the multiplexers, there are several other characteristics, as for example the dimensions and the coupling zones, which could influence the spectral output response of these devices.

Regarding the output of a wavelength multiplexer, this device can be an optoelectronic device if a photodetector is implemented in the system or an optical device as part of an optical system or application such as an optical filter, amplifier, switch, source, among others.

Moreover, to do the assessment of wavelength multiplexers for telecommunications, the choice of the optical bands is essential. In this research, the analysis happened in the range between 1420 nm until 1620 nm, being considered only 4 optical bands, the E-band (1360 nm – 1460 nm), the S-band (1460 nm – 1530 nm), the C-band (1530 nm – 1565 nm) and the L-band (1565 nm – 1625 nm).

1.2 Objectives

The main goal of this research is to analyse and characterize the output response of wavelength multiplexer systems, namely ring resonators with planar optical waveguides by doing a parameter study using the finite element method. To first characterize the optical systems of ring resonators, it is fundamental to present the essential concepts regarding light propagation in optical waveguides and their fundamental structures. Moreover, the analysis of the parameters that influence the output response will be decisive depending on the requirements of each application and technologies for WDM. The program used for the numerical simulations of the optical systems is *COMSOL Multiphysics v5.4*. Also, to obtain the analytical models of the ring resonators, *MATLAB R2020a* is the program used.

1.3 Outline

Taking into account the objectives presented, this document is structured into eight chapters.

The **first** chapter is the **introduction,** which covers the main aspects underlying wavelength division multiplexing systems. Likewise, the objectives and the structure of the document are presented.

The **second** chapter is known as **light propagation and optical waveguides**, where is presented the basics of wave theory in planar optical waveguides and a brief description of the Coupled Mode theory.

The **third** chapter is the **state-of-the-art review**. The historical context and development, the parameters, and the basic topologies of the ring resonator optical systems are stated and described.

The **fourth** chapter includes the main procedures of the **finite element method** as well as the ***COMSOL Multiphysics*** *v5.4* configurations for the numerical simulations of the add-drop ring resonator systems.

The chapters **5, 6 and 7** contains the **numerical simulations** of the optical systems, namely ring resonators, using a parameter study based on the finite element method implemented for planar optical waveguides. For the **fifth** chapter, the first simulated model of the add-drop ring resonator is considered and described, taking into account the procedures of the finite element method in *COMSOL*. In the sections of the fifth chapter, the output responses of the simulated ring resonators models are studied, considering different parameters and the **analytical models** obtained. In the sixth and seventh chapters, distinct systems of ring resonators, with 2 and 3 ring-shaped waveguides, are represented and described by the analytical method and the output responses are presented and analysed.

The **eighth** chapter presents the **conclusions** of this research with some aspects for future analysis.

2

Light Propagation and Optical Waveguides

The wave description of light was firstly introduced in the 19th century by Maxwell's equations [6,7]. This set of equations are the basis to understand the relationship between the magnetic and electrical fields and how their interaction allows the light wave to propagate at the speed of light, c_0, in vacuum. Later, Hertz experimentally confirmed the existence of electromagnetic waves and determined the wavelength of the radiation and the propagation velocity of electromagnetic waves.

The light wave propagation can be analysed considering the Maxwell's equations in a homogeneous, isotropic and a **lossless dielectric** medium. The relation between the magnetic field, $\boldsymbol{H}$, and the electrical field, $\boldsymbol{E}$, is given by the differential equations 2.1 and 2.2, where ε_0 is the electric permittivity in vacuum, μ_0 is the magnetic permeability in vacuum and the refractive index of the medium is represented by *n*. At vacuum, it is considered that *n* is unitary.

$$\nabla \times \boldsymbol{E} = -\mu_0 \frac{\partial \boldsymbol{H}}{\partial t} \tag{2.1}$$

$$\nabla \times \boldsymbol{H} = \varepsilon_0 n^2 \frac{\partial \boldsymbol{E}}{\partial t} \tag{2.2}$$

In this case, light waves can be considered as **plane waves** [8] and the magnetic and electric fields can be represented by sinusoidal functions, characterized by an amplitude and an angular frequency ω. Moreover, considering a wave propagation along the ***z*** axis, the electric and magnetic fields are presented, being $\overline{\boldsymbol{E}}(z)$ and $\overline{\boldsymbol{H}}(z)$ the electric and magnetic phasors, respectively:

$$\boldsymbol{E}(z,t) = Re\{\overline{\boldsymbol{E}}(z)\, e^{j\omega t}\},\ \overline{\boldsymbol{E}}(z) = E_r\, e^{-j\beta z}, \tag{2.3a}$$

$$\boldsymbol{H}(z,t) = Re\{\overline{\boldsymbol{H}}(z)\, e^{j\omega t}\},\ \overline{\boldsymbol{H}}(z) = H_r\, e^{-j\beta z}. \tag{2.3b}$$

Taking into account the phasors representation of the fields with a propagation constant *β* and a complex amplitude accordingly to the position *r* in the normal plane of the z axis, it is fundamental to define the boundary conditions when the refractive index *n* changes, that is, when the medium changes. For lossless mediums, the tangential components of each field must be equal at the boundaries.

The differential equations 2.1 and 2.2 can be rewritten in rectangular coordinates considering the equations 2.3a and 2.3b into the following, for the analysis of the two-dimensional slab waveguides:

$$\begin{cases} \frac{\partial E_z}{\partial y} + j\beta E_y = -j\omega\mu_0 H_x, \\ -j\beta E_x - \frac{\partial E_z}{\partial x} = -j\omega\mu_0 H_y, \\ \frac{\partial E_y}{\partial x} - \frac{\partial E_x}{\partial y} = -j\omega\mu_0 H_z, \end{cases} \tag{2.4}$$

$$\begin{cases} \frac{\partial H_z}{\partial y} + j\beta H_y = j\omega\varepsilon_0 n^2 E_x, \\ -j\beta H_x - \frac{\partial H_z}{\partial x} = j\omega\varepsilon_0 n^2 E_y, \\ \frac{\partial H_y}{\partial x} - \frac{\partial H_x}{\partial y} = j\omega\varepsilon_0 n^2 E_z. \end{cases} \tag{2.5}$$

Moreover, light propagation occurs not only in vacuum or free-space regions, but also light can be confined in structures known as optical fibers or optical waveguides.

The two-dimensional, 2D, structure of an optical waveguide presents a core inside a cladding and/or a substrate [9]. These 2 sections of the waveguide have 2 different refractive indexes, allowing the light to be reflected at the core, that has a higher refractive index, n_{core} (n_1), when compared to the cladding's refractive index, n_{clad} (n_0). The total reflection of the light only happens if the incident angle of the light wave, θ, represented in the Figure 2.1, is lower than the maximum light acceptance angle, θ_{max}.

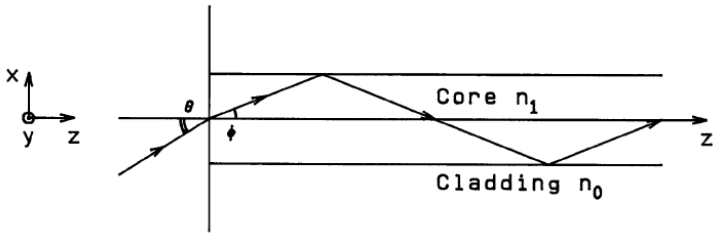

Figure 2.1 – Basic structure of a two-dimensional optical waveguide (from [6]).

The θ_{max} and the maximum inclination angle within the core, ϕ_{max}, can be obtained with the calculus of the relative refractive index, Δ, taking into account the equations 2.6, 2.7 and 2.8:

$$\Delta = \frac{n_{core}^2 - n_{clad}^2}{2n_{core}^2}, \tag{2.6}$$

$$\theta_{max} = n_{core}\sqrt{2\Delta}, \tag{2.7}$$

$$\sin\theta_{max} = n_{core}\ \sin\phi_{\max}. \tag{2.8}$$

Even if θ is smaller than the θ_{max}, light waves will only propagate inside the waveguide with a certain discrete inclination angle ϕ, dependent on the waveguide structure such as the core radius, the core refractive index and the relative refractive index. This inclination angle, ϕ, also depends on the wavelength of the light, λ_0, defined as the ratio between c_0 and the frequency *f*. For each ϕ there is a distinct optical field called the mode. The fundamental mode is given by the minimum inclination angle.

The propagation constant, *β*, of the light wave is defined by the equation 2.9, being the wavenumber of the light represented by *k*, defined as the ratio between 2π and the vacuum wavelength λ_0.

$$\beta = k\, n_{core}\cos\phi = k\, n_{eff}. \tag{2.9}$$

As a replacement for ϕ, the constant *β* can be also obtained by the effective refractive index, n_{eff}.

Furthermore, two-dimensional slab waveguides are characterized by having three main parts such as the core, the cladding, and the substrate, each one with a distinct refractive index [10]. These two-dimensional slab waveguides can be symmetric if $n_{sub} = n_{clad}$ or asymmetric if $n_{sub} \neq n_{clad}$. In this specific case, considering the set of equations 2.4 and 2.5, the electric and magnetic fields are independent of the y-axis, as it can be observed in the Figure 2.1, where it is considered the plane *xz*. Therefore, in slab waveguides only exist two independent modes, which are the transversal electric, TE, mode, where there is only electric field alongside the y-axis, and the transversal magnetic, TM, mode, where there is only magnetic field alongside the y-axis.

The TE and TM modes must accomplish the following wave equations 2.10a and 2.10b, respectively, considering the derivative $\partial/\partial y = 0$ for the electric and magnetic fields.

$$\frac{d^2E_y}{dx^2} + (k^2n^2 - \beta^2)E_y = 0 \tag{2.10a}$$

$$\frac{1}{n^2}\frac{d^2H_y}{dx^2} + \left(k^2 - \frac{\beta^2}{n^2}\right)H_y = 0 \tag{2.10b}$$

Furthermore, the equations 2.3 and 2.4 can be simplified for the TE and TM modes into the following,

$$\text{TE:} \begin{cases} H_x = -\frac{\beta}{\omega\mu_0}E_y \\ H_z = \frac{j}{\omega\mu_0}\frac{dE_y}{dx} \\ E_x = E_z = H_y = 0 \end{cases} \tag{2.11}$$

$$\text{TM:} \begin{cases} E_x = \frac{\beta}{\omega\varepsilon_0 n^2}H_y \\ E_z = -\frac{j}{\omega\varepsilon_0 n^2}\frac{dH_y}{dx} \\ E_y = H_x = H_z = 0. \end{cases} \tag{2.12}$$

Taking into account these TE and TM modes and the equations 2.11 and 2.12, it is essential to determine the dispersion equations. The power applied in the waveguide is also a parameter to define each mode.

To do three-dimensional theoretical analysis of waveguides, particularly rectangular waveguides, one of the methods is proposed by Marcatili in the 20th century [11]. Regarding this method, the main approximation is the disregard of the electromagnetic field in most of the cladding area of the waveguide. According to this analysis, there are multiple modes divided into two main situations. First, where the magnetic field in the x axis is neglected and, secondly, where the magnetic field in the y axis is neglected. Taking into account this assumptions and situations, the dispersion equations are found.

The Kumar's method [12] is another procedure to analyse rectangular waveguides. This time, the refractive index of the total cladding area is not neglected and can be approximated to n_{clad}. Despite this approximation, it is useful to use the perturbation method, with separation of variables, to fully estimate the dispersion equations, the constant of propagation β and the electromagnetic field distribution.

The analytical methods described for the rectangular waveguides are just approximations. Despite these previous methods, with the effective index method it is possible to simplify the analysis of three-dimensional waveguide structures onto two-dimensional structures. The finite element method, FEM, is appliable for more complex 2D or three-dimensional waveguide structures considering WDM.

The implementation of basic optical couplers has the coupled mode theory as theoretical basis to investigate the interactions of two or more light waves used in real WDM technologies and applications.

The first coupled mode theory description was made by Pierce and Miller in 1954 [13]. In the following years, this theory was developed and applied by other authors in optical waveguides and fiber optics. The models for the coupling scenarios are characterized by having two or more dielectric waveguides. Likewise, to introduce the coupled mode theory, it is considered a basic model, consisting of a directional coupler with two parallel waveguides, characterized by the respective propagation constants, β_1 and β_2. The electric and magnetic fields can be defined by the linear superposition of the waveguide modes.

The optical couplers are divided into codirectional and contra directional couplers, regarding the direction of the light propagation in the waveguides. Additionally, it is possible to define other essential parameters of the couplers such as the coupling length, ℓ, and the maximum power coupling efficiency, η. Assuming the example of 2 codirectional coupled waveguides with a real coefficient κ, this parameters can be expressed by the following expressions, 2.13 and 2.14, in which δ is defined as half the difference between the propagation constants of each waveguide. If the propagation constants are equal, $\eta = 1$.

$$\eta = \frac{1}{1+ (\delta/\kappa)^2} \tag{2.13}$$

$$\ell = \frac{\pi}{2\sqrt{\kappa^2+\delta^2}} \tag{2.14}$$

These parameters depend on the structure and on the guided modes of each coupled waveguide. Also, the determination of these parameters is useful to analyse different optical devices based on couplers.

Two examples of coupler devices are the Mach-Zehnder interferometers [14] and the ring resonators [15]. The interferometers and the ring resonators are made of straight and curved waveguides structures. In these coupler devices, the optical phase ϕ is responsible for the output change in terms of the optical intensity in the interferometers and the optical transmittance in the ring resonators.

The so-called Mach-Zehnder interferometer can be represented by the Figure 2.2.

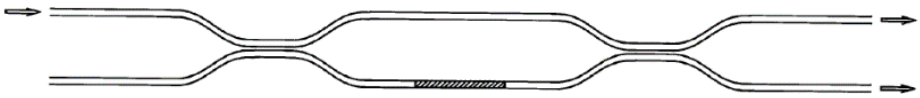

Figure 2.2 – Representation of a Mach-Zehnder interferometer (from [6]).

Moreover, an optical ring resonator can be represented by the Figure 2.3.

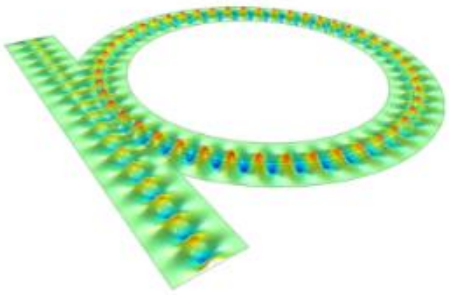

Figure 2.3 – Representation of an optical ring resonator (from [16]).

3

State-of-the-Art

For WDM technologies, one type of coupler devices that can be used is the ring resonator, RR. Ring resonators are built with distinct sizes, from a few meters to micrometers, and with different types of materials depending on the application requirements such as the output spectrum and the finesse [17]. In this case, the micro ring resonators, MRR, are the most important for integration in larger devices, particularly for applications in optics, such as switching [18, 19, 20], or photonics, as for example in biosensors [21] and lasers [22]. These type of optical resonators can operate also as filters [23], where the input wavelength signals are distributed in straight and curved waveguides or optical fibers, [24]. Marcatili was responsible for the simulation of an integrated ring resonator for a filter in 1969 [25].

The development of optical ring resonators began with the demonstration of the first guided optical RR by Weber and Ulrich in 1971 [26, 27, 28]. In 1980, Haavisto and Pajer fabricated a RR with low loss in the waveguides, which are coupled with a larger curved region, of a few cm, via the evanescent field [29]. Two years later in 1982, the first optical glass fiber RR was built by Stokes, Chodorow, and Shaw. From this decade onwards, ring resonators were made with glass as the main material and other components that allow the change of the glass refractive index. There are also several studies with another ring resonators with silica-based glasses [30, 31, 32] and polymers [33, 34] in the past years.

In 1997, Rafizadeh et al. fabricated a MRR with a lateral coupling to bus waveguides. Afterwards, it was demonstrated that this MRR can be used in several applications in multi-ring devices, switches and for WDM [35]. Other technologies such as micro disks resonators, tunable ring resonators with other types of couplers were also developed and demonstrated with different sizes in recent years [36,37,38].

RR can have numerous configurations. However, it is crucial to define the 2 basic configurations to further analyse complex devices. These 2 configurations have one or two straight waveguides, also called port/bus waveguides, and a ring-shaped waveguide, which is **evanescently coupled**. The single RR and the add-drop RR can be represented by Figures 3.1 and 3.2, respectively.

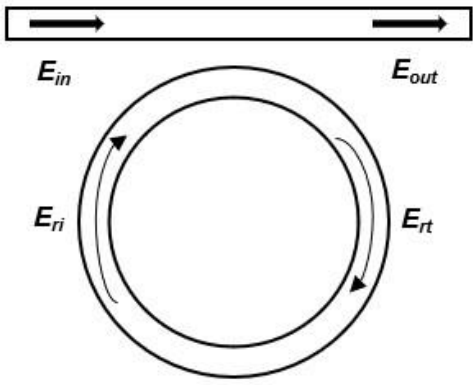

Figure 3.1 – Single RR.

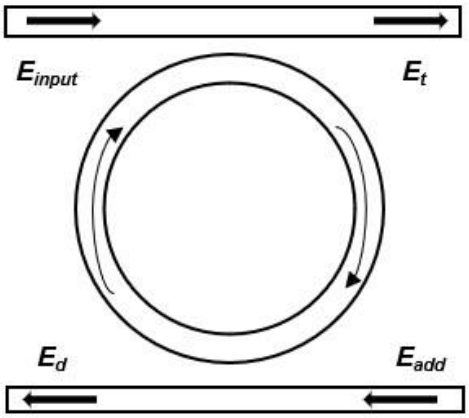

Figure 3.2 – Add-drop RR.

To simplify the analysis of ring resonators, it is considered that the input power is equal to the output power, that is, the coupling is lossless and the light inside the waveguides are partially transmitted in the coupling region. Regarding the simplification, the scattering matrix can be used to describe the fields.

Firstly, considering the single RR, the scattering matrix is defined as in equation 3.1, being $\overline{\boldsymbol{E}}_{\boldsymbol{out}}$ and $\overline{\boldsymbol{E}}_{\boldsymbol{in}}$ the output field and the input field of the bus waveguide, respectively. Moreover, the fields inside the ring-shaped waveguide, $\overline{\boldsymbol{E}}_{\boldsymbol{ri}}$ and $\overline{\boldsymbol{E}}_{\boldsymbol{rt}}$, can also be related taking into account the equation 3.2.

$$\begin{bmatrix} \overline{\boldsymbol{E}}_{\boldsymbol{out}} \\ \overline{\boldsymbol{E}}_{\boldsymbol{rt}} \end{bmatrix} = \sqrt{1-\gamma} \begin{bmatrix} A & jB \\ jB & A \end{bmatrix} \begin{bmatrix} \overline{\boldsymbol{E}}_{\boldsymbol{in}} \\ \overline{\boldsymbol{E}}_{\boldsymbol{ri}} \end{bmatrix} \tag{3.1}$$

$$\overline{\boldsymbol{E}}_{\boldsymbol{ri}} = \tau\, e^{-j\phi} \overline{\boldsymbol{E}}_{\boldsymbol{rt}} \tag{3.2}$$

The scattering matrix is symmetrical with real coupling coefficients *A* and *B*, that are related by:

$$A^2 + B^2 = 1. \tag{3.3}$$

The amplitude transmission factor τ is given by $\tau = \exp(-\rho L/2)$, being ρ the amplitude attenuation coefficient and *L* is the perimeter of the ring-shaped waveguide, given by $L = 2\pi r$, with a radius, *r*, of the exterior circumference of the ring-shaped waveguide. The optical phase ϕ is given by $\phi = \beta L + \phi_0$, where β is defined by the product between the wavenumber *k* and the effective index, n_{eff}, and ϕ_0 is the additional phase shift. Also, the amplitude loss coefficient is represented by γ.

Considering the relationships of the fields, the ratio between the output and input fields is given by:

$$\frac{\overline{\boldsymbol{E}}_{\boldsymbol{out}}}{\overline{\boldsymbol{E}}_{\boldsymbol{in}}} = \sqrt{1-\gamma}\, \left[\frac{A - \sqrt{1-\gamma}\, \tau\, e^{-j\phi}}{1 - A\sqrt{1-\gamma}\, \tau\, e^{-j\phi}} \right] \tag{3.4}$$

The amplitude transmittance defined by equation 3.4 is the basis to obtain the intensity transmittance factor *T*, which allows to characterize the transmission of the RR as a function of the optical phase ϕ. The transmittance factor is expressed below, in which the parameter x is given by $x = \sqrt{1-\gamma}\, \tau$.

$$T(\phi) = \left| \frac{\overline{\boldsymbol{E}}_{\boldsymbol{out}}}{\overline{\boldsymbol{E}}_{\boldsymbol{in}}} \right|^2 = (1-\gamma) \left[\frac{A^2 + x^2 - 2Ax\cos\phi}{1 + A^2x^2 - 2Ax\cos\phi} \right] \tag{3.5}$$

According to the transmittance factor expression above, the maximum and minimum values for *T* are:

$$T_{max} = (1-\gamma) \frac{(A+x)^2}{(1+Ax)^2} \tag{3.6a}$$

$$T_{min} = (1-\gamma) \frac{(A-x)^2}{(1-Ax)^2} \tag{3.6b}$$

The minimum transmittance factor is obtained at resonance, defined when $\phi = 2\pi m$, where m is an integer. Moreover, the *T* factor at resonance becomes zero when A = x, that is, the coupling losses matches the internal losses. In this case, there is no transmission of light, and the RR is critically coupled.

Regarding the add-drop RR configuration, there are 4 ports, known as the input port, throughput port, drop port and add port. Considering the coupling and loss coefficients of the second bus waveguide as A_2, B_2 and γ_2, the throughput port field, $\overline{\boldsymbol{E}}_{\boldsymbol{t}}$, is presented, being $\overline{\boldsymbol{E}}_{\boldsymbol{input}}$ and $\overline{\boldsymbol{E}}_{\boldsymbol{add}}$ the input port field and the add port field, respectively. The drop port field, $\overline{\boldsymbol{E}}_{\boldsymbol{d}}$, is given with the exchange of the fields.

$$\overline{\boldsymbol{E}}_{\boldsymbol{t}} = \sqrt{1-\gamma}\, \left[\frac{A - A_2\sqrt{1-\gamma_2}\, x\, e^{-j\phi}}{1 - A_2\sqrt{1-\gamma_2}\, A\, x\, e^{-j\phi}} \right] \overline{\boldsymbol{E}}_{\boldsymbol{input}} - \frac{BB_2\sqrt{1-\gamma}\sqrt{1-\gamma_2}\, \sqrt{\tau}\, e^{-j\phi/2}}{1 - A_2\sqrt{1-\gamma_2}\, A\, x\, e^{-j\phi}}\, \overline{\boldsymbol{E}}_{\boldsymbol{add}} \tag{3.7}$$

$$\bar{E}_d = \sqrt{1-\gamma}\left[\frac{A - A_2\sqrt{1-\gamma_2}\,x\,e^{-j\phi}}{1 - A_2\sqrt{1-\gamma_2}\,A\,x\,e^{-j\phi}}\right]\bar{E}_{add} - \frac{BB_2\sqrt{1-\gamma}\sqrt{1-\gamma_2}\sqrt{\tau}\,e^{-j\phi/2}}{1 - A_2\sqrt{1-\gamma_2}\,A\,x\,e^{-j\phi}}\,\bar{E}_{input} \quad (3.8)$$

The transmittance factors for the add-drop RR configuration, taking into account only the input port, for the throughput port and the drop port are presented, in which the parameter x_2 is given by $x_2 = \sqrt{1-\gamma_2}$.

$$T_{through}(\phi) = \left|\frac{\bar{E}_t}{\bar{E}_{input}}\right|^2 = (1-\gamma)\left[\frac{A^2 + A_2^2x_2^2x^2 - 2AA_2x_2x\cos\phi}{1 + A_2^2A^2x^2x_2^2 - 2AA_2x_2x\cos\phi}\right] \quad (3.9)$$

$$T_{drop}(\phi) = \left|\frac{\bar{E}_d}{\bar{E}_{input}}\right|^2 = (1-\gamma)\left[\frac{(1-A^2)(1-A_2{}^2)\,x_2^2\tau}{1 + A_2^2A^2x^2x_2^2 - 2AA_2x_2x\cos\phi}\right] \quad (3.10)$$

At resonance, and taking into account only the input port, the transmittance of the throughput port becomes zero if the add-drop RR is lossless, ρ = γ = γ_2 = 0, and if the couplers coefficients are equal.

Beyond the determination of the transmittance factors, in both configurations, as the fundamental output response as function of the wavelength λ, the radius *r* and the effective index; RRs can be analysed and characterized by other important four figures of merit, like the free spectral range, FSR, the resonance width or full width at half maximum, FWHM, the finesse, *F*, and the quality factor, *Q*.

The *FSR* is defined as the difference between two consecutive resonance wavelengths. This figure of merit can also be defined as in the equation 3.12, being the derivative of the propagation constant *β*, considering the resonance wavelength, λ_{res}, as expressed in equation 3.11.

$$\frac{\partial\beta}{\partial\lambda} = -\frac{k}{\lambda_{res}}n_g = -\frac{k}{\lambda_{res}}\left(n_{eff} - \lambda_{res}\frac{\partial n_{eff}}{\partial\lambda}\right) = -\frac{\beta}{\lambda_{res}} + k\frac{\partial n_{eff}}{\partial\lambda} \quad (3.11)$$

$$\mathrm{FSR} = -\frac{2\pi}{L}\left(\frac{\partial\beta}{\partial\lambda}\right)^{-1} = \frac{\lambda_{res}^2}{n_gL} \quad (3.12)$$

The group refractive index is represented by n_g.

The FWHM can be defined as δλ in terms of wavelength. This parameter depends on the configuration used for the RR. The expression of the FWHM for the add-drop RR is given in equation 3.13.

$$\mathrm{FWHM} = \delta\lambda = \frac{\lambda_{res}^2}{\pi\,L\,n_{eff}}\,\frac{(1-xx_2AA_2)}{\sqrt{xx_2AA_2}} \quad (3.13)$$

The finesse, *F*, can be obtained from the ratio between the FSR and the FWHM, and the quality factor, *Q*, can be expressed as function of the finesse, defined in equation 3.14, as given in equation 3.15.

$$F = \frac{\mathrm{FSR}}{\mathrm{FWHM}} \quad (3.14)$$

$$Q = \frac{\lambda_{res}}{\mathrm{FWHM}} = \frac{\lambda_{res}}{\mathrm{FSR}}F = \frac{n_gL}{\lambda_{res}}F \quad (3.15)$$

In addition to considering these parameters above and the theoretical description of the RRs, it is fundamental to describe the finite element method and the program behind the simulations of the RRs.

4

Finite Element Method and *COMSOL Multiphysics*

The concept of FEM has been present since 1960, when it was first used by Clough [39, 40] in his paper. Although, this method started to be developed by Courant [41] and Hrenikoff [42] over structural projects. Initially, the FEM was applied for solid and fluid mechanics in a steady-state analysis before the widespread use in a variety of engineering problems, reported by Zienkiewicz and Cheung in 1965 [43]. Nowadays it is possible to find numerous software programs based on the FEM and capable of design all sort of complex geometries, for a wider range of applications and engineering fields, like electromagnetism and acoustics, to analyse time-independent and propagation problems.

The FEM is a numerical method in which the partial difference equations, PDE, that rule a complex system are approximated by the junction of elements defined by simpler equations. These elements are obtained by space discretization of the system, considering its initial and boundary conditions represented in nodal points, where the field variables of the system are known. The choice of the number and geometry of the elements and the simpler equations may depend on the desired minimum error.

Despite the criterium for the minimization of the error, the finite elements can be obtained taking into account 3 possible procedures. The direct procedure applies to steady-state problems, where the algebraic equations are determined via numerical algebra. The variational procedure applies to transient problems, where the ordinary difference equations are determined via numerical integration. The third and more general procedure relies on the weighted residuals, based on the Galerkin method, where the approximation error of the FEM is minimized by selecting the adequate trial and weight functions [44].

Moreover, the FEM can be applied on a system by doing an analysis, characterized by 3 steps [45].

The first step, known as pre-processing, consists of designing the complex geometry of the system, defining the material properties, the boundary conditions, given the field variables, and discretizing the system by creating a mesh. The mesh can have different types of 2D or 3D elements depending on the order of the interpolation functions. Often, these functions are polynomials with order zero for constants, with order one for linear functions or even with order two for quadratic functions. The second order elements are normally described with curved edges at the boundaries and a higher number of nodes. The second step, known as processing, consists of establishing the procedure to determine the equations for each element of the system and then solving the equations for the entire system, obtaining the field variables defined at the nodal points. The final step, known as post-processing, consists of analysing the results, such as the field variables, surface and 2D plots, and testing the model for different parameters, by changing the material properties and the boundary conditions, for example.

Considering the advantages of the FEM for application in complex systems, this method is the basis to characterize and analyse WDM optical systems, using the *COMSOL Multiphysics* software.

The first WDM optical system taking into consideration is the add-drop ring resonator example of the state-of-the-art. For this ring resonator, the 3 steps of the analysis are presented in detail. For the other WDM optical systems, only the geometry and the material properties are presented and described.

Before the description and analysis of the optical systems based on ring resonators, it is essential to introduce the main configurations of the *COMSOL Multiphysics* used for the RR models simulated.

To describe and examine an RR model, firstly, the global parameters are defined in the model builder. Then, a component is created with the definitions including the boundary system and the global variable probes, which are the variables required to do the analysis of the optical systems afterwards. The geometry of the optical system is also established, and the physics are determined by the wave optics module, designed to help solving electromagnetic wave problems regarding optical applications [46].

The physics interface chosen is The Electromagnetic Waves, Frequency Domain Interface (*ewfd*). This interface is needed for systems with plane waves, in which the fields are seen as phasors. Furthermore, the electric field is determined as a three-component vector with a formulation of a full field as default. Moreover, in this interface, 9 nodes are added for the description of the equations and boundaries. The first node is the Wave Equation, Electric 1, where is it defined the equation and the electric displacement field model. The equation for this node is presented below in equation 4.1 for boundary mode analysis.

$$\nabla \times (\nabla \times \boldsymbol{E}) - k^2 n^2 \boldsymbol{E} = 0 \tag{4.1}$$

The refractive index is the electric displacement field selected, being user defined for the real part as the core refractive index, n_{core}, and for the imaginary part as zero, being both isotropic. The second node is the Wave Equation, Electric 2, stated with the same equation and the same electric displacement field employed apart from using the real part of the substrate refractive index, n_{sub}. The initial null values for the electric field components are indicated in the third node known as Initial Values. The other 6 nodes are relative to the boundaries and ports of the system, defined as perfect electric conductors. The Port 1 is the only input port of the RR system and there is a scattering boundary condition.

After the creation of the component branch, the formed study is determined by a parametric sweep of wavelengths. For each wavelength, a frequency domain is performed with the reference frequency and a boundary mode analysis is made for each port with 1 desired mode and a mode search around n_{core}. The mesh is a physics-controlled mesh with a maximum element size governed by the study.

The final branch of the model builder is known as the results, which includes the data sets of the solutions, the tables, and the plots of the global variables defined in the component branch. As part of the physics interface, it is also possible to obtain the electric field profile and the output transmittances of the RR systems. These transmittances are equal to the square modulus of the scattering parameters. These S-parameters are used for optical analysis with high frequencies as defined in *COMSOL*.

Moreover, for the refractive index definition, the materials library of the *COMSOL* can be used as well.

In annex B, the model builder scheme used for all optical systems is presented.

5

Add-drop RR: Description and Analysis

5.1 Description and analysis of the first simulated model

The add-drop RR is the first optical system characterized taking into account the FEM for the WDM analysis. In this initial step, the ring-shaped waveguide is represented with a circle and an inner layer at the centre of the substrate which is defined as a square. The 2 straight waveguides are represented as rectangles with the same height as the substrate and the same width defined as *w*. These waveguides are located considering the thickness *w*, the distance *d,* and the radius *r* of the ring-shaped waveguide. The geometrical model for the add-drop RR is represented in *COMSOL Multiphysics* by Figure 5.1.

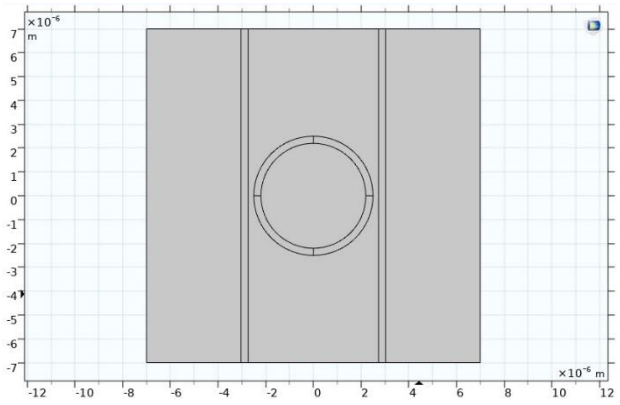

Figure 5.1 – Geometrical model for the add-drop RR.

Besides the geometrical model of the add-drop RR, the domains of the system are defined for the processing. For the add-drop RR, there are 3 domains with different fundamental equations; the core domain with a real refractive index n_{core}, the substrate domain with a real refractive index n_{sub}, and the boundary domain defined as a perfect electric conductor which has no internal electric field. The 4 ports are represented in the boundary domain being the Port 1 the input port where occurs the wave excitation. Considering the domains for the system, the mesh is created with extremely fine triangular elements. The physical domains and the mesh created for the add-drop RR are represented as in Figure 5.2.

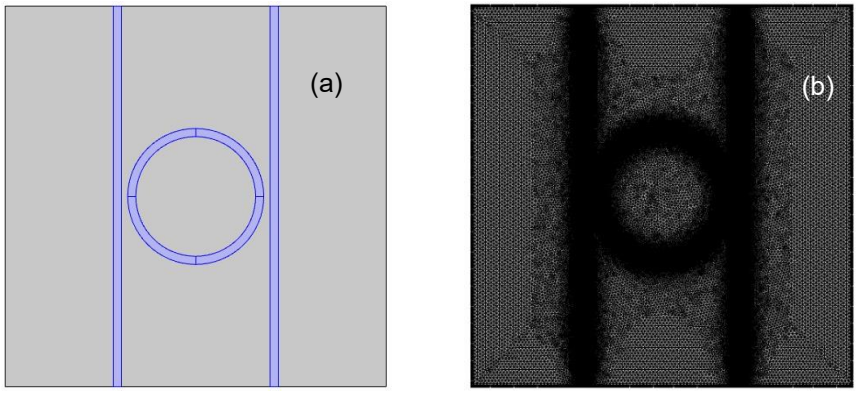

Figure 5.2 – (a): Core (blue) and substrate (grey) domains, (b): Triangular Mesh

The post-processing of the add-drop RR consists of a parametric sweep, as well as 4 boundary mode analysis and a frequency domain for 1000 points. This number of results is necessary taking into account the order of magnitude of the interval of wavelengths required.

For the first numerical simulation, the dimensions of the RR are defined by a radius, *r*, of the ring-shaped waveguide, with 2,5 μm, a distance, *d*, between waveguides of 0,232 μm and a thickness, *w*, of 0,3 μm for each waveguide. The refractive indexes of the waveguides, n_{core} and n_{sub}, are equal to 3,2 and 1, respectively. The reference wavelength is equal to 1 μm, being f_0, the reference frequency. Besides, the add-drop RR can be represented by Figure 5.3, with a substrate square area of 196 μm^2.

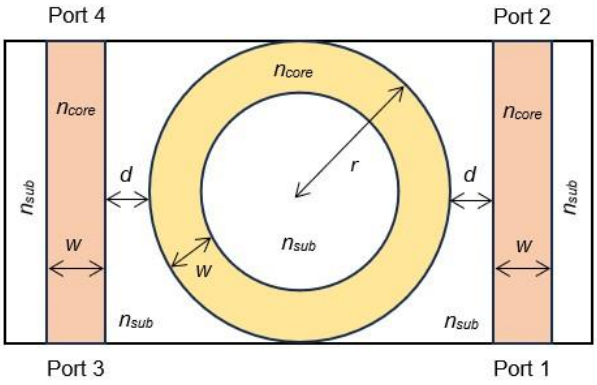

Figure 5.3 – The 2D representation of the add-drop RR for the numerical simulation.

After making the representation of the add-drop RR, the wave and boundary equations, the initial values for the fields, and the 4 ports are defined, being the port 1 the input port with an injected power of 1 W (reference power). To analyse and obtain the transmittances of the RR, a parametric sweep, a boundary mode analysis for each port and a frequency domain study are performed for each wavelength. For the parametric sweep, the wavelength is specified from 1420 nm to 1620 nm, with an interval of 0,2 nm for each result. The boundary mode analysis is implemented considering the effective mode index for two-dimensional problem analysis. The transmittances of the output ports 2 and 3, the throughput and drop ports, respectively, of the RR are given by Figure 5.4, being represented as function of the wavelength.

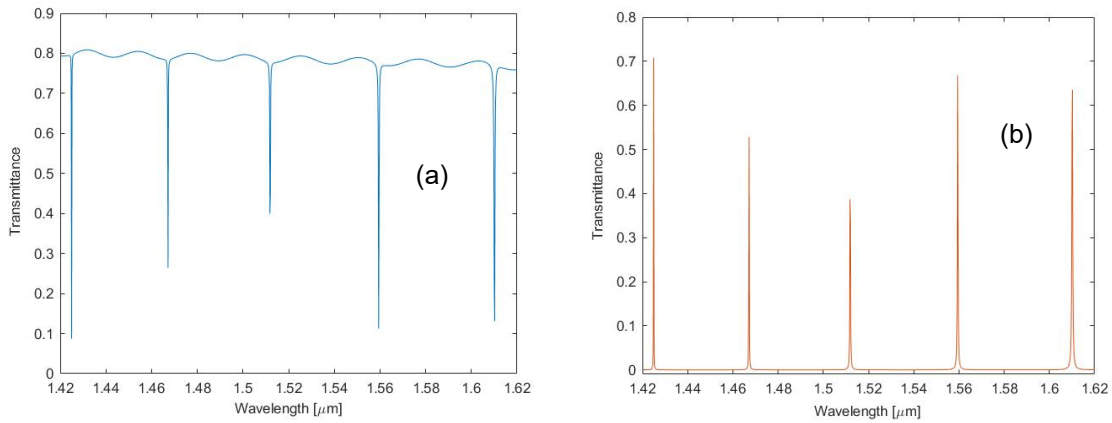

Figure 5.4 – Transmittances of the add-drop RR: (a) – port 2, (b) – port 3.

Taking into account the Figure 5.4 and the results from the numerical simulation, the transmittance of the throughput port is around 0.8 in almost all wavelengths, except for the 5 resonant peaks. Regarding the drop port, the transmittance is practically zero, except for the same resonant wavelengths. These results show that this add-drop RR is capable of filtering and splitting the signal, as expected, considering previous analysis of the RR performance based on the theoretical basis by Hiremath [47,48].

5.2 Determination of the parameters for the analytical model

Considering the transmittance results and the theoretical equations 3.9 and 3.10 from the state-of-the-art for the add-drop RR, it is now possible to determine the coupling and loss coefficients and obtain the analytical model of the add-drop RR. For this model, it is considered that the intensity loss coefficients are equal for both couplers, $\gamma = \gamma_2$. As defined in the state-of-the-art, the resonance occurs when the phase shift ϕ is a multiple of 2π, that is, the cos ϕ is unitary and the transmittance is minimum for the throughput port and maximum for the drop port. When the cos ϕ is equal to -1, the transmittance is maximum for the throughput port and minimum for the drop port. Therefore, the maximum and minimum transmittances for the ports 2 and 3 can be defined by the equations 5.1, 5.2, 5.3 and 5.4.

$$T_{2_{max}} = (1-\gamma)\frac{(A+A_2(1-\gamma)\tau)^2}{(1+AA_2(1-\gamma)\tau)^2} \quad (5.1)$$

$$T_{2_{min}} = (1-\gamma)\frac{(A-A_2(1-\gamma)\tau)^2}{(1-AA_2(1-\gamma)\tau)^2} \quad (5.2)$$

$$T_{3_{max}} = (1-\gamma)\frac{(1-A^2)(1-{A_2}^2)(1-\gamma)\tau}{(1-AA_2(1-\gamma)\tau)^2} \quad (5.3)$$

$$T_{3_{min}} = (1-\gamma)\frac{(1-A^2)(1-{A_2}^2)(1-\gamma)\tau}{(1+AA_2(1-\gamma)\tau)^2} \quad (5.4)$$

The values of the T_{2min} and the T_{3max} are determined by doing the mean of the transmittances obtained in resonance for each port. The T_{2max} is determined by the mean of the maximum transmittances obtained in between two resonance peaks for port 2. The T_{3min} is determined by the mean of the minimum transmittances obtained in between two resonance peaks for port 3. Considering the results obtained for this model, the transmittances and the means obtained are presented in the Table 5.1.

Table 5.1 – Add-drop RR: Maximum, minimum transmittances and means values.

Minimums of T_2	Maximums of T_3	Maximums of T_2	Minimums of T_3
0,08726	0,70811	0,80859	1,2768 x 10^{-5}
0,26465	0,52823	0,80010	2,8377 x 10^{-5}
0,39955	0,38687	0,79355	4,2393 x 10^{-5}
0,11252	0,66806	0,78576	7,6940 x 10^{-5}
0,13135	0,63530	0,76384	3,1861 x 10^{-4}

$T_{2_{min}}$	$T_{3_{max}}$	$T_{2_{max}}$	$T_{3_{min}}$
0,19997	0,58531	0,79037	9,4918 x 10^{-5}

Taking into account the mean results from the Table 5.1 and knowing that the coupling coefficients have a modulus less than 1 and the amplitude transmission factor, τ, is a real positive number, there are 2 possible solutions for both coupling coefficients, being $|A| \approx 0{,}9811$ and $|A_2| \approx 0{,}9937$, and a unique solution for the losses, with $\tau \approx 1{,}265$ and $\gamma \approx 0{,}2095$, being the coupling lossless with $(1-\gamma)\,\tau \approx 1$.

Besides the determination of the coupling and loss coefficients, it is also necessary to obtain the optical phase, ϕ, to calculate the transmittance of the throughput and drop ports for each wavelength defined in the parametric sweep. For this reason, the effective refractive index, n_{eff}, and the additional phase shift, ϕ_0 must be determined. These 2 parameters are calculated considering the resonance condition of the phase shift, being 2π the distance between 2 resonance peaks. Consequently, the effective refractive index, n_{eff}, and the additional phase shift ϕ_0 are determined by the equations 5.5 and 5.6, being *m,* the index of the resonance wavelength considered, taking into account the indexes of the Table 5.2.

$$n_{eff} = \frac{1}{L\left(\frac{1}{\lambda_m} - \frac{1}{\lambda_{m+1}}\right)} \tag{5.5}$$

$$\phi_0 = 2\pi \left(1 - \frac{n_{eff}\, L}{\lambda_m}\right) \tag{5.6}$$

As in this case there are more than 2 resonance peaks, the effective refractive index is a mean value considering all resonance wavelengths presented in the Table 5.2. The additional phase shift can be obtained from any resonance wavelength. In this scenario, it is chosen the first resonance wavelength.

Table 5.2 – Resonance wavelengths of the add-drop RR.

λ_1	λ_2	λ_3	λ_4	λ_5
1,4250 µm	1,4672 µm	1,5118 µm	1,5594 µm	1,6102 µm

Considering the Table 5.2 and the equations 5.5 and 5.6, $n_{eff} \approx 3{,}1150$ and $\phi_0 \approx -33{,}778 * 2\pi$.

Through the calculus of the coefficients and parameters for the application of the equations 3.9 and 3.10, the transmittances of the ports 2 and 3 for the analytical model can be represented by Figure 5.5.

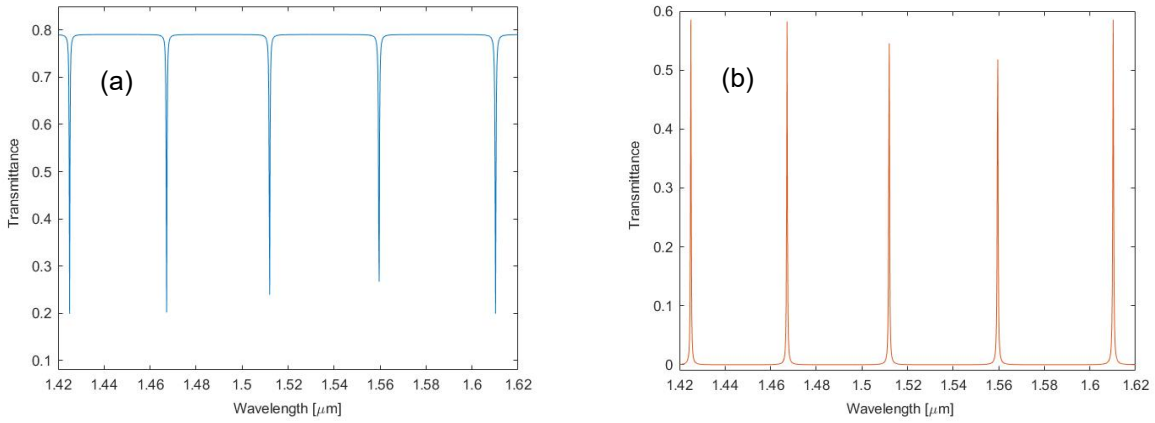

Figure 5.5 – Transmittances of the RR for the analytical model: (a) – port 2, (b) – port 3.

5.3 Description and analysis of models with different radii

In addition to considering the add-drop RR with a radius, *r*, of 2,5 μm, it is also examined 2 other models with smaller radii. The 2 chosen radii for the models are 2,0 μm and 1,5 μm. All the other dimensions are kept the same as much as the physical domains defined and the post-processing procedures.

The transmittances of the output ports 2 and 3, the throughput and drop ports, respectively, of the RR with a radius of 2,0 μm are given by Figure 5.6, being represented as function of the wavelength.

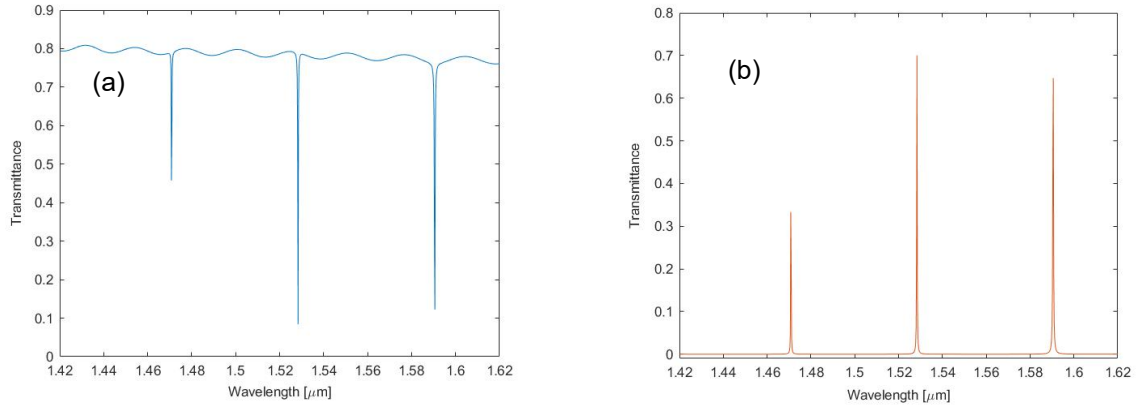

Figure 5.6 – Transmittances of the RR with a radius of 2,0 μm: (a) – port 2, (b) – port 3.

The transmittances of the output ports 2 and 3, the throughput and drop ports, respectively, of the RR with a radius of 1,5 μm are given by Figure 5.7, being represented as function of the wavelength.

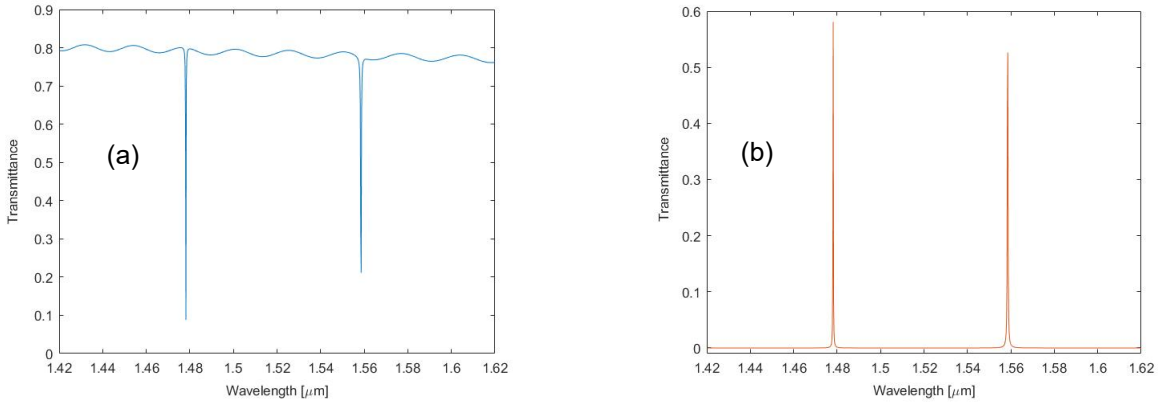

Figure 5.7 – Transmittances of the RR with a radius of 1,5 μm: (a) – port 2, (b) – port 3.

The procedures to obtain the analytical model for this 2 cases are the same as before with less resonance wavelengths in both cases. For the add-drop RR model with a radius of 1,5 μm, the number of resonance peaks is the minimum possible to calculate the effective refractive index n_{eff}. Considering the results obtained for these models, the resonance wavelengths are presented in the Table 5.3.

Table 5.3 – Resonance wavelengths of the add-drop RRs with different radii.

RR with radius **2,0 μm**	$\lambda_1 = 1{,}4708$ μm	$\lambda_2 = 1{,}5284$ μm	$\lambda_3 = 1{,}5906$ μm
RR with radius **1,5 μm**	$\lambda_1 = 1{,}4782$ μm	$\lambda_2 = 1{,}5586$ μm	

Considering the Table 5.3 and the equations 5.5 and 5.6, for the RR with a radius of 2,0 μm, n_{eff} ≈ 3,1080 and ϕ_0 ≈ -25,554 * 2π and for the RR with a radius of 1,5 μm, n_{eff} ≈ 3,0405 and ϕ_0 ≈ -18,386 * 2π.

For this RRs, the maximum and minimum transmittances of the output ports are presented in Table 5.4.

Table 5.4 – Maximum and minimum transmittances for the RR with distinct radii.

RR with radius **2,0 μm**	Minimums of T_2	0,45775	0,08400	0,12223
	Maximums of T_2	0,80048	0,78860	0,77967
	Maximums of T_3	0,33298	0,70044	0,64707
	Minimums of T_3	2,0513 x 10^{-5}	3,5057 x 10^{-5}	6,4221 x 10^{-5}
RR with radius **1,5 μm**	Minimums of T_2	0,08819	0,21140	
	Maximums of T_2	0,79707	0,78486	
	Maximums of T_3	0,58076	0,52639	
	Minimums of T_3	1,1418 x 10^{-5}	2,9663 x 10^{-5}	

The mean values of the transmittances for both simulated models are presented in Table 5.5.

Table 5.5 – Mean values of the transmittances for the RR models with different radii.

	RR with radius **2,0 μm**	RR with radius **1,5 μm**
$T_{2_{min}}$	0,22134	0,14980
$T_{2_{max}}$	0,78958	0,79098
$T_{3_{max}}$	0,56016	0,55357
$T_{3_{min}}$	3,9930 x 10^{-5}	2,0540 x 10^{-5}

Taking into account the results from the Table 5.5 for both models, and knowing that the coupling coefficients have a modulus less than 1 and that the coupling is lossless, there are 2 possible solutions for both coupling coefficients in both models, being |A| ≈ 0,9872 and |A_2| ≈ 0,9961 for the RR model with a radius of 2,0 μm, and being |A| ≈ 0,9913 and |A_2| ≈ 0,9970 for the RR with a radius of 1,5 μm.

For the loss coefficients, there are a unique solution in both models, with τ ≈ 1,266 and γ ≈ 0,2104, for the RR with a radius of 2,0 μm, and with τ ≈ 1,264 and γ ≈ 0,2090, for the other RR analytical model.

Through the calculus of the necessary coefficients and parameters, the transmittances of the ports 2 and 3 for the analytical model of the RR with a radius of 2,0 μm can be represented by the Figure 5.8.

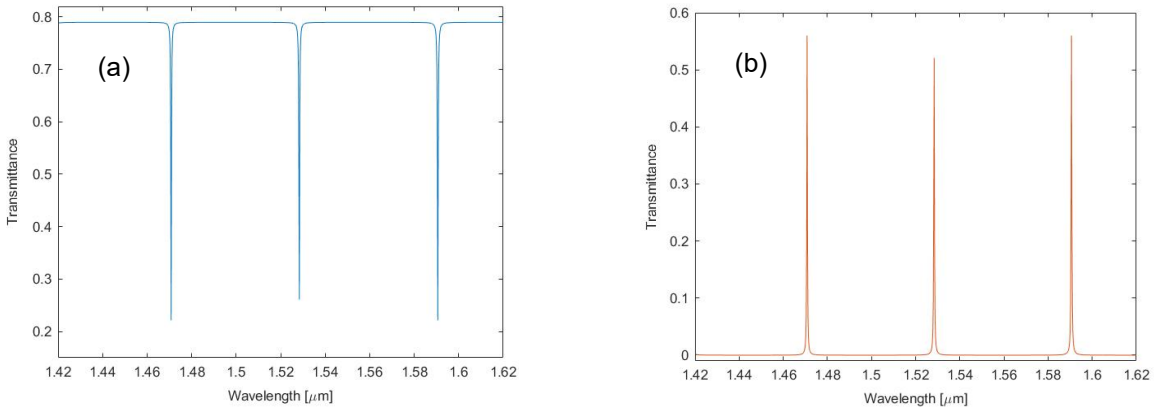

Figure 5.8 – Transmittances of the analytical RR with a radius of 2,0 μm - (a): port 2, (b): port 3.

For the analytical model of the RR with a radius of 1,5 μm, the transmittances of the throughput and drop ports, considering the calculated coefficients, can be represented by the Figure 5.9.

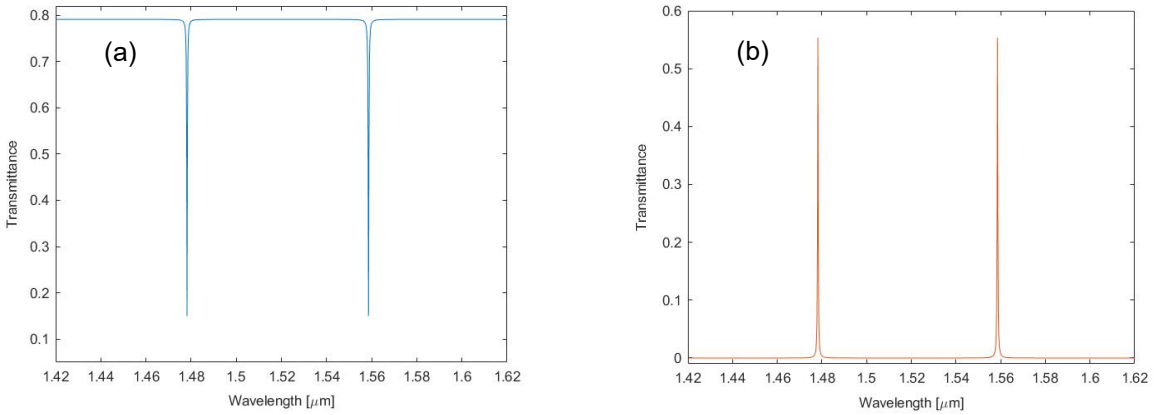

Figure 5.9 – Transmittances of the analytical RR with a radius of 1,5 μm - (a): port 2, (b): port 3.

Taking into account the transmittance results of the analytical models and the simulated models of the add-drop RR for all the radii analysed, as the radius decreases, the number of resonance wavelengths is minor. Thus, the change of the radius of the ring-shaped waveguide permits the tuning of the number of output resonance wavelengths of the add-drop RR. It is also noticed that the maximum transmittance of the throughput port in all cases is around 80%, thanks to the insertion loss of each coupler. The analytical resonance wavelengths are the same as the simulated ones as expected considering ϕ_0. The difference between the results of the analytical models and of the simulated models, for the values of the transmittance in resonance, are due to the mean values assumed for the calculus of the coefficients and the approximate solutions obtained. For the simulated models, the throughput transmittance in non-resonance wavelengths oscillate around 0.8 due to the finite element method calculation procedures.

Despite the determination of the analytical models of the add-drop ring resonators, it is essential to obtain the FSR, the FWHM, the finesse and the quality factor to better characterize the add-drop RRs.

Hence and considering the equations for the 4 parameters mentioned, defined in the state-of-the-art, the results, in terms of the resonance wavelengths for each model, are presented in Table 5.6, considering the loss coefficients equal, $\gamma = \gamma_2$, and the simplification of the group index: $n_g \approx n_{eff}$.

Table 5.6 – The results of the FSR, FWHM, *Q*, and *F* for the RRs with different radii.

RR Model	λ_m [µm]	Δλ [nm]	δλ [nm]	*Q*	*F*
RR with radius **2,5 µm**	$\lambda_1 = 1{,}4250$	40,975	0,33221	4289,5	123,34
	$\lambda_2 = 1{,}4672$	43,437	0,35217	4166,1	
	$\lambda_3 = 1{,}5118$	46,118	0,37391	4043,2	
	$\lambda_4 = 1{,}5594$	49,068	0,39783	3919,8	
	$\lambda_5 = 1{,}6102$	52,317	0,42417	3796,1	
RR with radius **2,0 µm**	$\lambda_1 = 1{,}4708$	55,388	0,29772	4940,2	186,04
	$\lambda_2 = 1{,}5284$	59,812	0,32150	4754,0	
	$\lambda_3 = 1{,}5906$	64,779	0,34820	4568,1	
RR with radius **1,5 µm**	$\lambda_1 = 1{,}4782$	76,253	0,29570	4998,9	257,87
	$\lambda_2 = 1{,}5586$	84,773	0,32875	4741,0	

Taking into account the results from the Table 5.6, as the resonance wavelength increases for each model with different radii, the FSR increases as expected considering the equation 3.12, defined in the state-of-the-art. The FSR can also be obtained by the calculus of the difference between 2 consecutive resonance wavelengths, which give more accurate results. Despite this approach, the absolute errors are just of a few nanometres. The FWHM can also be defined as the bandwidth regarding each resonance peak. As observed, with the rise of the resonance wavelength within each model, the FWHM increases and the quality factor decreases, as projected. Furthermore, the finesse is specified for each RR model, being higher for the models with smaller radii, due to the FSR increase.

For a better visualization of the differences between the simulated and analytical results, the transmittances of the ports 2 and 3, for the models with distinct radii, are presented in Figure 5.10.

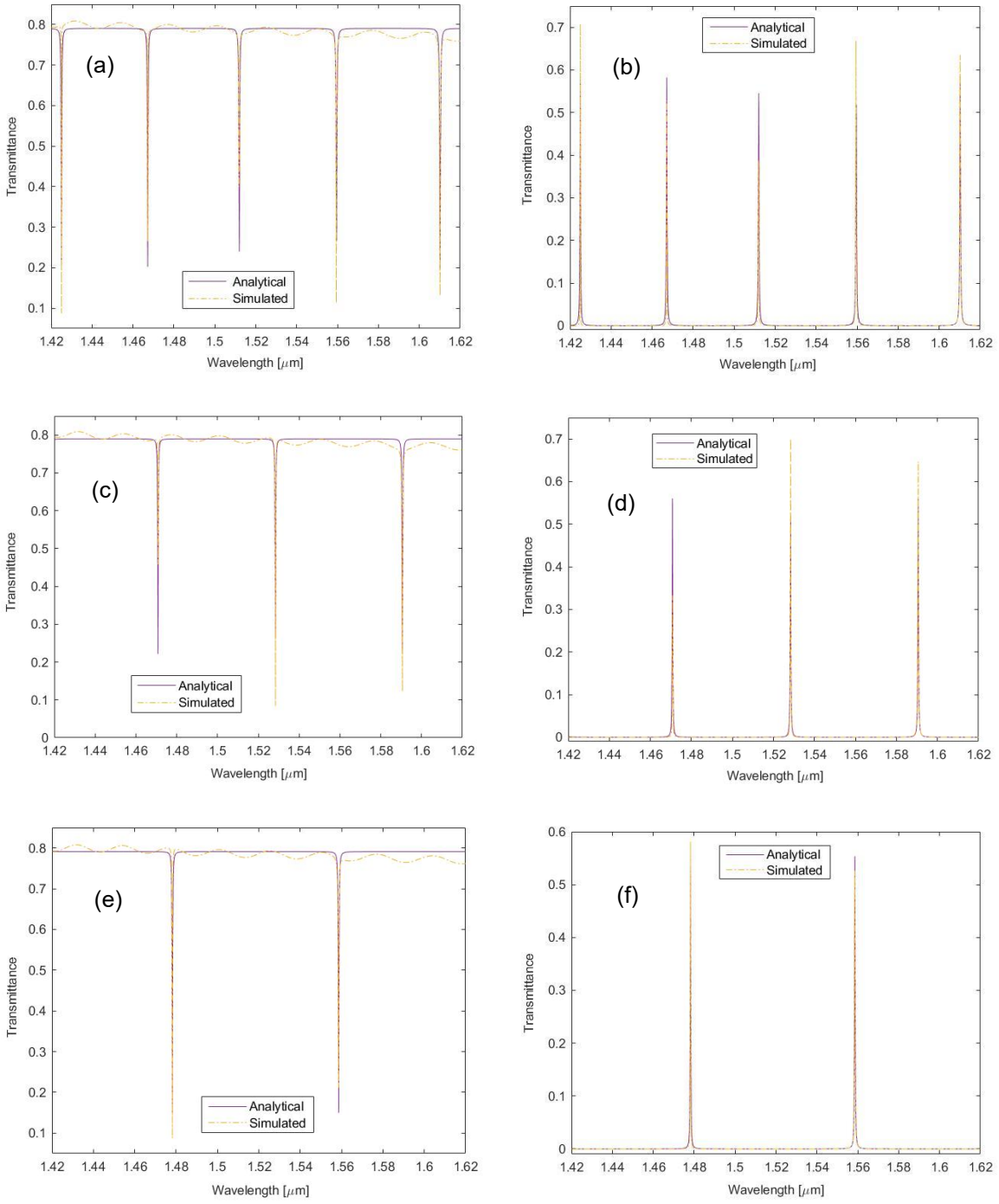

Figure 5.10 – Transmittances of the RR models with distinct radii:

(a) – port 2 and (b) – port 3 : RR model with a radius of 2,5 μm;

(c) – port 2 and (d) – port 3 : RR model with a radius of 2,0 μm;

(e) – port 2 and (f) – port 3 : RR model with a radius of 1,5 μm.

5.4 Description and analysis of models with distinct core materials

In addition to considering the models of the add-drop RR with distinct radii, it is also examined 2 other models with different core materials. These materials can be optically characterized by their complex refractive index, which depend on the chosen wavelength. In this models, the wavelength considered is the centre wavelength of the optical analysis, λ = 1,52 μm, and the imaginary part of the refractive index for both materials can be neglected. Thus, the 2 chosen materials, modelled by Marple [49,50] in 1964, are the zinc selenide, ZnSe, with a real refractive index of 2,45 and the cadmium telluride, CdTe, with a real refractive index of 2,74. All the other parameters, such as the refractive index of the substrate, n_{sub}, are kept the same as much as the physical domains defined and the post-processing procedures.

The transmittances of the output ports 2 and 3, the throughput and drop ports, respectively, of the RR with a n_{core} = 2,45 are given by Figure 5.11, being represented as function of the wavelength.

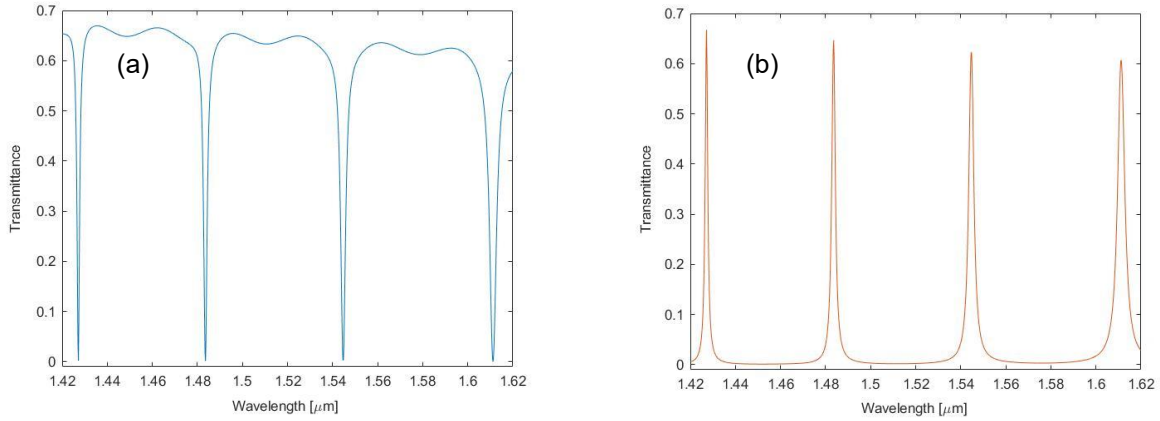

Figure 5.11 – Transmittances of the RR with a n_{core} = 2,45: (a) – port 2, (b) – port 3.

The transmittances of the output ports 2 and 3, the throughput and drop ports, respectively, of the RR with a n_{core} = 2,74 are given by the Figure 5.12, being represented as function of the wavelength.

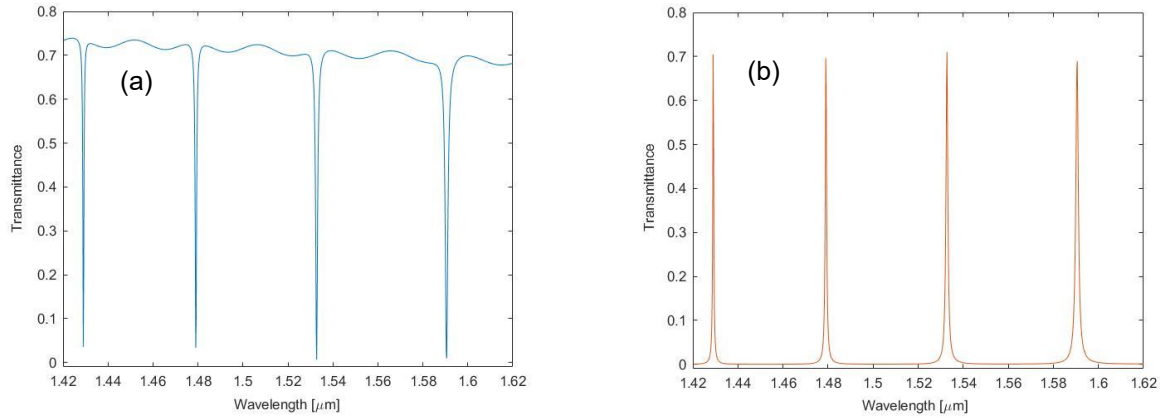

Figure 5.12 – Transmittances of the RR with a n_{core} = 2,74: (a) – port 2, (b) – port 3.

The procedures to obtain the analytical models for this 2 cases with different materials, and 4 resonance wavelengths, are the same as for the other models with distinct radii. Considering the results obtained for these models with different materials, the resonance wavelengths are presented in the Table 5.7.

Table 5.7 – Resonance wavelengths of the add-drop RRs with distinct core materials.

RR with n_{core} of **2,45**	$\lambda_1 = 1{,}4272$ μm	$\lambda_2 = 1{,}4836$ μm	$\lambda_3 = 1{,}5446$ μm	$\lambda_4 = 1{,}6112$ μm
RR with n_{core} of **2,74**	$\lambda_1 = 1{,}4290$ μm	$\lambda_2 = 1{,}4790$ μm	$\lambda_3 = 1{,}5328$ μm	$\lambda_4 = 1{,}5906$ μm

Considering the Table 5.7 and the equations 5.5 and 5.6, for the RR with a n_{core} of 2,45, $n_{eff} \approx 2{,}3868$ and $\phi_0 \approx -25{,}2697 * 2\pi$ and for the RR with a n_{core} of 2,74, $n_{eff} \approx 2{,}6863$ and $\phi_0 \approx -28{,}5285 * 2\pi$.

The maximum and minimum transmittances of the output ports for this RRs are presented in Table 5.8.

Table 5.8 – Maximum and minimum transmittances for the RRs with distinct core materials.

RR with n_{core} **2,45**	Minimums of T_2	0,00195	0,00117	0,00258	$4{,}099 \times 10^{-5}$
	Maximums of T_2	0,66947	0,65420	0,63577	0,57974
	Maximums of T_3	0,66764	0,64680	0,62267	0,60721
	Minimums of T_3	0,00127	0,00194	0,00324	0,02824
RR with n_{core} **2,74**	Minimums of T_2	0,03545	0,03327	0,00665	0,00941
	Maximums of T_2	0,73500	0,72416	0,71057	0,69873
	Maximums of T_3	0,70458	0,69544	0,71027	0,68953
	Minimums of T_3	$2{,}473 \times 10^{-4}$	$4{,}373 \times 10^{-4}$	$6{,}5995 \times 10^{-4}$	0,00109

The mean values of the transmittances for both RR models are presented in Table 5.9.

Table 5.9 – Mean values of the transmittances for the RR models with distinct materials.

	RR with n_{core} of **2,45**	RR with n_{core} of **2,74**
$T_{2_{min}}$	0,00144	0,02120
$T_{2_{max}}$	0,63480	0,71712
$T_{3_{max}}$	0,63608	0,69996
$T_{3_{min}}$	0,00867	$6{,}0860 \times 10^{-4}$

Taking into account the results from the Table 5.9 for both models and the same conditions as before, there are 2 possible solutions for both coupling coefficients, being $|A| \approx 0{,}8844$ and $|A_2| \approx 0{,}8952$ for the RR model with a n_{core} of 2,45 and being $|A| \approx 0{,}9660$ and $|A_2| \approx 0{,}9758$ for the RR with a n_{core} of 2,74.

For the loss coefficients, there are a unique solution for both models, with $\tau \approx 1{,}552$ and $\gamma \approx 0{,}3565$, for the RR with a n_{core} of 2,45, and with $\tau \approx 1{,}3935$ and $\gamma \approx 0{,}2823$, for the other RR analytical model.

Through the calculus of the necessary coefficients and parameters, the transmittances of the ports 2 and 3 for the analytical model of the RR with a n_{core} of 2,74 can be represented by the Figure 5.13.

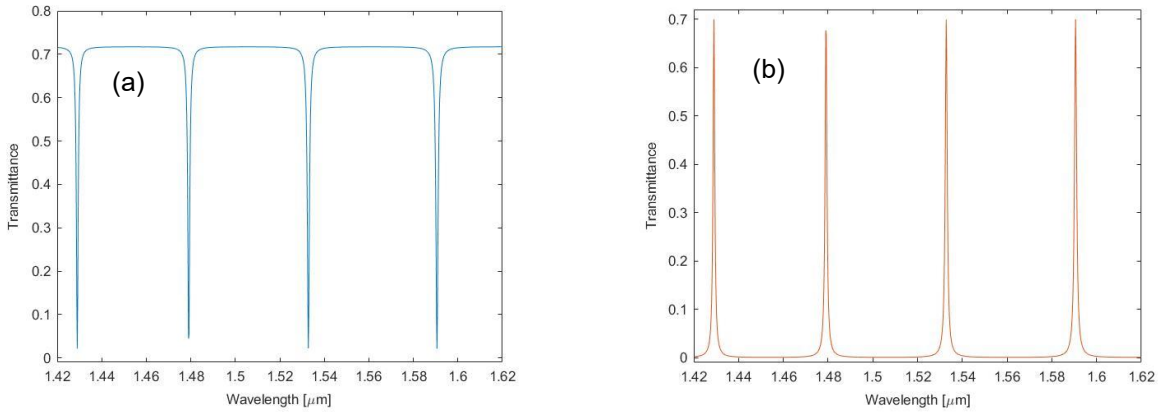

Figure 5.13 – Transmittances of the analytical RR with a n_{core} of 2,74: (a) – port 2, (b) – port 3.

For the analytical model of the RR with a n_{core} of 2,45, the transmittances for the throughput port and for the drop port, considering the calculated coefficients, can be represented by the Figure 5.14.

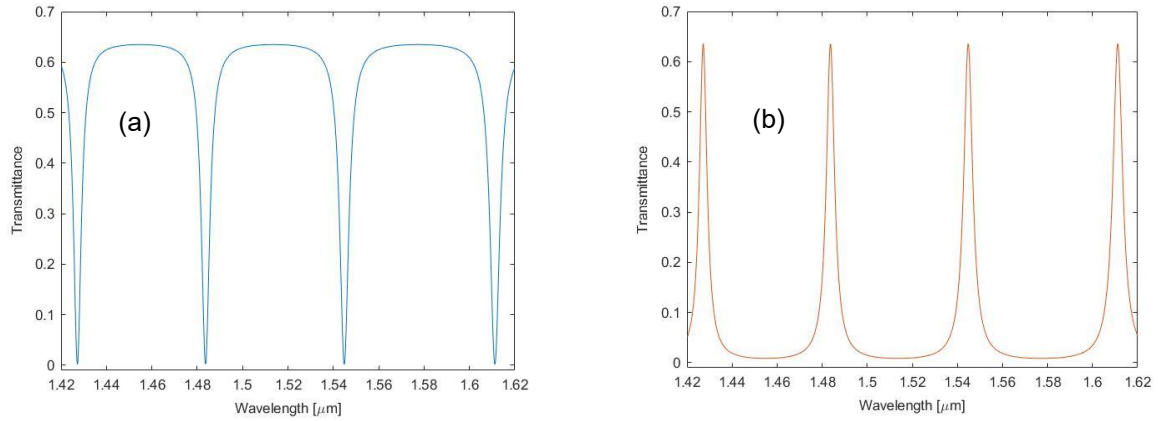

Figure 5.14 – Transmittances of the analytical RR with a n_{core} of 2,45: (a) – port 2, (b) – port 3.

Taking into account the results of the analytical models and the simulated models of the add-drop RR for all the core materials chosen, as the n_{core} decreases, the maximum transmittance decreases from around 72 % to 63 %, for the throughput port and from around 70 % to 64 % for the drop port in resonance. Although the equal number of resonance wavelengths for both models, the resonance wavelengths are located elsewhere, as noticed in Table 3.7, with a higher FWHM for the model with a lower n_{core}. The analytical resonance wavelengths are the same as the simulated ones as expected considering ϕ_0. The difference between the results from the analytical and simulated models of the transmittance values in resonance are due to the mean values assumed for the calculus of the coefficients and the approximate solutions obtained. For the simulated models, the throughput transmittance in non-resonance wavelengths oscillate due to the FEM calculation procedures.

For this RR models with different materials, the FSR, the FWHM, the finesse and the quality factor are also determined. The results are presented in Table 5.10, considering the same simplifications as before.

Table 5.10 – The results of the FSR, FWHM, *Q*, and *F* for the RRs with varied core materials.

RR Model	λ_m [µm]	Δλ [nm]	δλ [nm]	*Q*	*F*
RR with n_{core} **2,45**	$\lambda_1 = 1{,}4272$	54,329	4,0660	351,01	13,3618
	$\lambda_2 = 1{,}4836$	58,707	4,3937	337,67	
	$\lambda_3 = 1{,}5446$	63,634	4,7623	324,33	
	$\lambda_4 = 1{,}6112$	69,240	5,1820	310,92	
RR with n_{core} **2,74**	$\lambda_1 = 1{,}4290$	48,394	0,9088	1572,3	53,2476
	$\lambda_2 = 1{,}4790$	51,840	0,9736	1519,2	
	$\lambda_3 = 1{,}5328$	55,680	1,0457	1465,8	
	$\lambda_4 = 1{,}5906$	59,958	1,1260	1412,6	

Taking into account the results from the Table 5.10, as the resonance wavelength increases for each model with different core materials, the FSR increases as expected considering the equation 3.12, defined in the state-of-the-art. For the models with different core materials, the absolute errors of the FSR are just of a few nanometres. As observed, with the increase of the resonance wavelength within each model, the FWHM increases and the quality factor decreases, as predicted considering the equations 3.13 and 3.15. Nonetheless, the FWHM of each resonance wavelength for the model with the lower refractive index is around 4 or 5 times higher than the FWHMs of the other model with a higher refractive index. Consequently, the quality factors are up to 4 or 5 times lower for the add-drop RR model with a lower refractive index. Furthermore, the finesse is specified for each RR model with a different material, being higher for the model with a higher refractive index, due to the lower FWHM in resonance.

The results of the add-drop RR models with different radii, of the ring-shaped waveguide, and with different core materials show that the FSR is the crucial parameter when considering the dimensions of the RR model and the FWHM is the fundamental parameter when considering the core material.

For a better visualization of the differences between the simulated and analytical results, the transmittances of the ports 2 and 3, for the models with distinct materials, are presented in Figure 5.15.

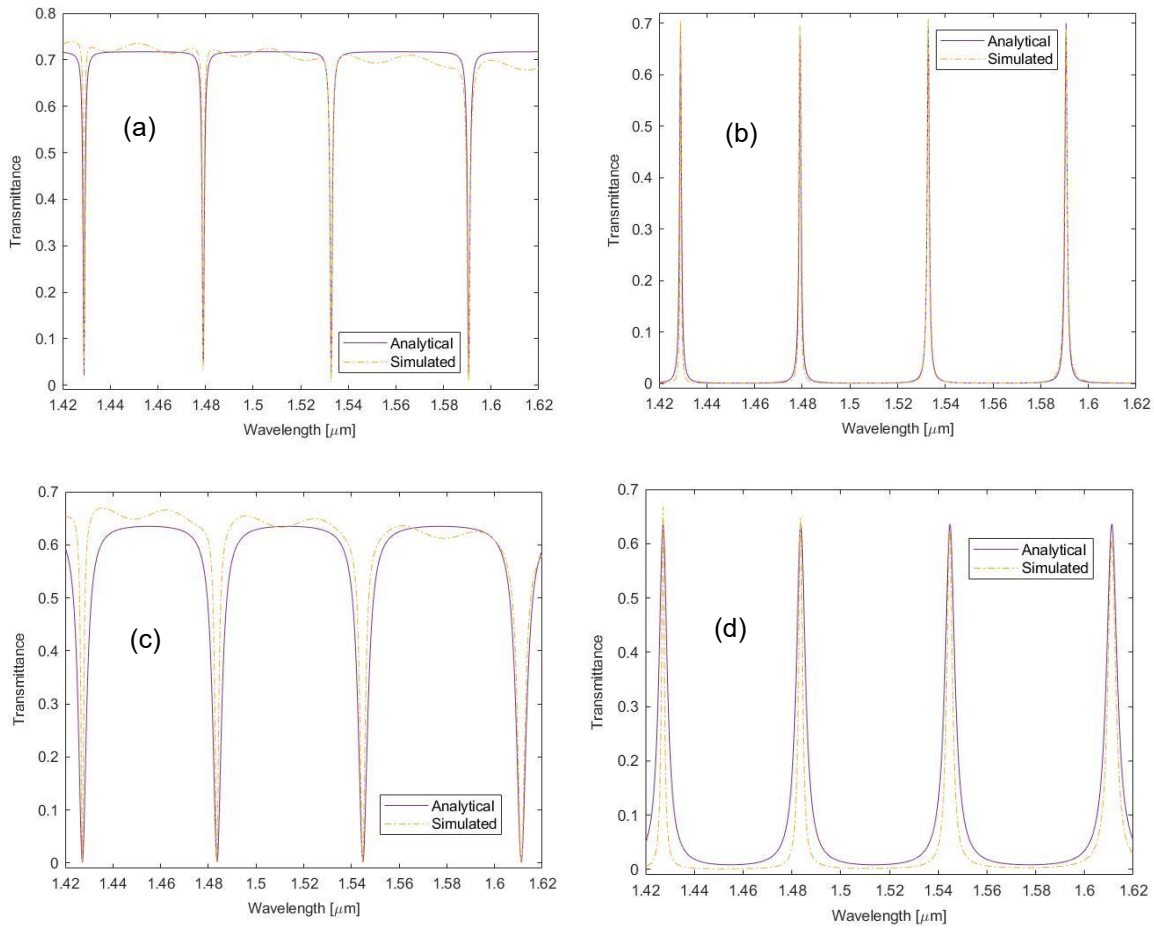

Figure 5.15 – Transmittances of the RR models with distinct materials:

(a) – port 2 and (b) – port 3 : RR model with a n_{core} of 2,74;

(c) – port 2 and (d) – port 3 : RR model with a n_{core} of 2,45.

Furthermore, the electric field profile of the add-drop RR model with a n_{core} of 2,74 can be represented by the Figure 5.16, considering a condition in resonance and another at the maximum transmittance.

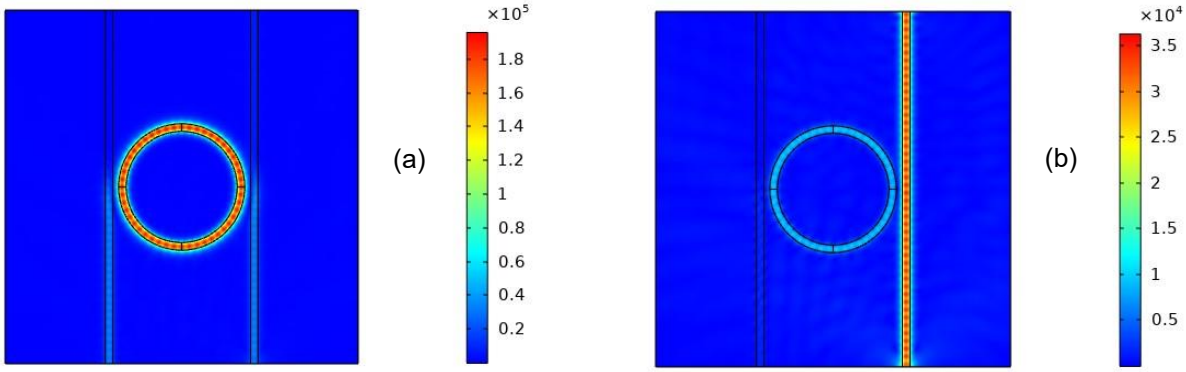

Figure 5.16 – Electric Field Profile in V/m of the add-drop RR model with a n_{core} of 2,74:

(a) - In resonance, $\lambda = 1{,}4290$ μm;

(b) - At the maximum transmittance of port 2, $\lambda = 1{,}4242$ μm.

5.5 Comparison of the models with distinct radii and core materials

Considering the results of the simulated add-drop RR models with different radii and core materials, the transmittances of the throughput and drop ports can be presented as seen in the Figure 5.17.

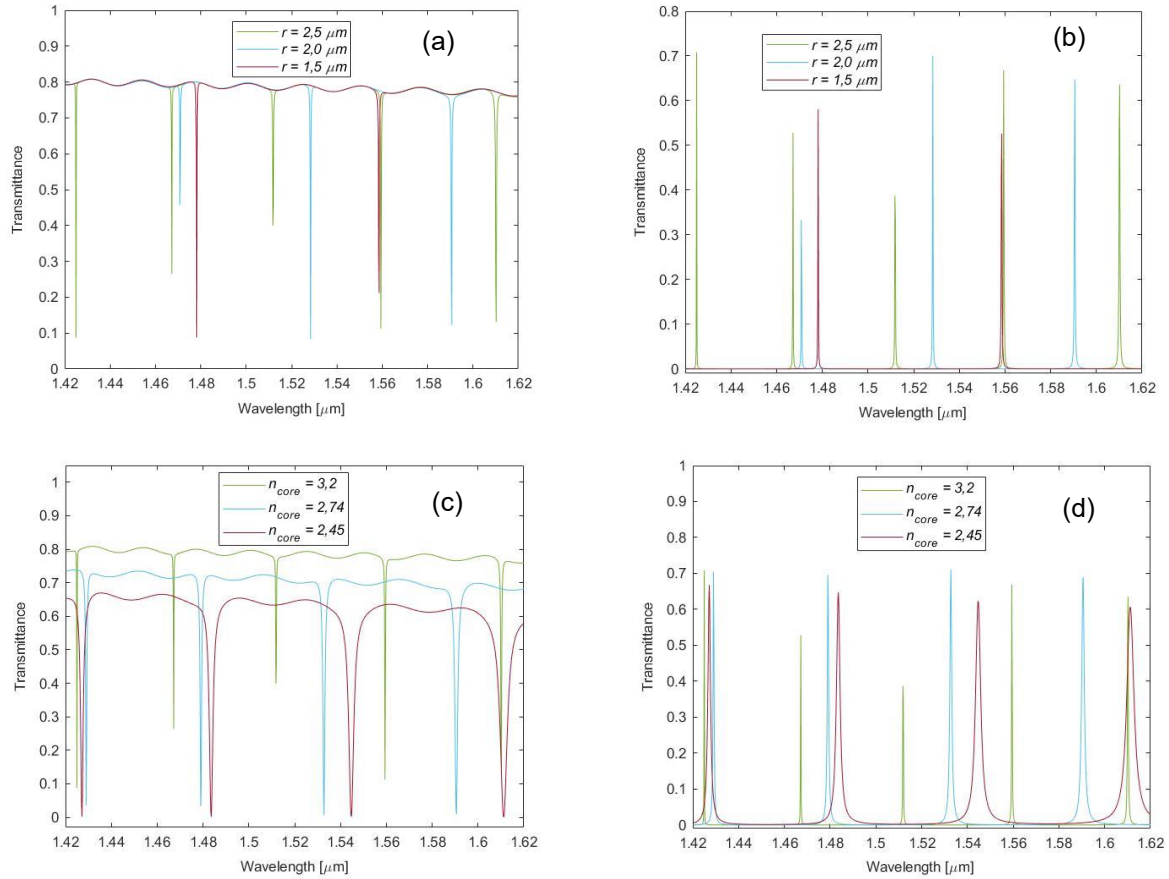

Figure 5.17 – Transmittances of the RR models with distinct parameters:

(a) – port 2 and (b) – port 3 : RR models with different radii;

(c) – port 2 and (d) – port 3 : RR models with different materials.

Taking into account the results for the distinct add-drop RR models with different parameters, the maximum transmittance is approximately equal for the add-drop RR models with different radii. However, the maximum and minimum transmittances drop with the decrease of the core refractive index. Despite the proximity between the first resonance peaks for the models with different materials, the other resonance peaks are easier to distinguish, due to the increased FSR for higher core refractive indexes.

The simulated add-drop RR models show that the modification of the dimensions for the ring-shaped waveguide and the change of the core material for all waveguides allow a distinct tuning of the output response, regarding the resonance wavelength location, and the maximum output transmittances.

6

Add-drop Double RR: Description and Analysis

The add-drop double RR, DRR, is the second optical system that is studied taking into account the analytical analysis and the FEM. This serially coupled RR model has one more ring-shaped waveguide than the previous add-drop RR model and its configuration can be represented by the Figure 6.1.

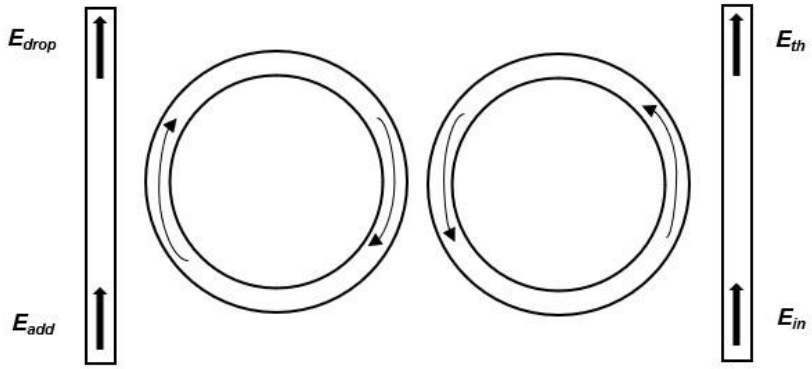

Figure 6.1 – Add-drop double RR.

To simplify the analytical analysis of the add-drop DRR, it is considered that the input power is equal to the output power, that is, the coupling is lossless and the light inside the waveguides are partially transmitted in the coupling region. Regarding the simplification and for this system onwards, the signal flow graph method [51,52] along with the Mason's rule can be used to describe the relation between the output and input fields. Therefore, the ratio between the drop field, $\overline{\boldsymbol{E}}_{\boldsymbol{drop}}$, and the input field, $\overline{\boldsymbol{E}}_{\boldsymbol{in}}$, and the ratio between the throughput field, $\overline{\boldsymbol{E}}_{\boldsymbol{th}}$, and the input field, $\overline{\boldsymbol{E}}_{\boldsymbol{in}}$, are given by:

$$\frac{\overline{\boldsymbol{E}}_{\boldsymbol{th}}}{\overline{\boldsymbol{E}}_{\boldsymbol{in}}} = \sqrt{1-\gamma}\left[\frac{A - A_2\,(1+AA_3)\,(1-\gamma)\tau\, e^{-j\phi} + A_3\,(1-\gamma)^2\tau^2\, e^{-j2\phi}}{1 - A_2\,(A+A_3)\,(1-\gamma)\tau\, e^{-j\phi} + AA_3\,(1-\gamma)^2\tau^2\, e^{-j2\phi}}\right], \tag{6.1}$$

$$\frac{\overline{\boldsymbol{E}}_{\boldsymbol{drop}}}{\overline{\boldsymbol{E}}_{\boldsymbol{in}}} = \sqrt{1-\gamma}\left[\frac{BB_2B_3(1-\gamma)\,\tau\, e^{-j\phi}}{1 - A_2\,(A+A_3)\,(1-\gamma)\tau\, e^{-j\phi} + AA_3\,(1-\gamma)^2\tau^2\, e^{-j2\phi}}\right]. \tag{6.2}$$

For simplification of the analytical model of the add-drop DRR, it is considered that the intensity loss coefficients are equal for all couplers, $\gamma = \gamma_2 = \gamma_3$. The real coupling coefficients are represented as A, A_2, A_3 and B, B_2 and B_3, which follow the same relation for each coupling defined by equation 3.3. The transmission factor τ and the optical phase ϕ are defined in the same way as presented in chapter 3.

Taking into account the equations 6.1 and 6.2, the *T* factors of the throughput and drop ports are given by the equations 6.3 and 6.4, being C_1, C_2 and C_3 real coefficients defined in equation 6.5.

$$T_{th}(\phi) = \left|\frac{\overline{\boldsymbol{E}}_{\boldsymbol{th}}}{\overline{\boldsymbol{E}}_{\boldsymbol{in}}}\right|^2 = (1-\gamma)\left[\frac{A^2 + {C_1}^2 + {C_2}^2 - 2C_1\,(A+C_2)\,\cos(\phi) + 2AC_2\,\cos(2\phi)}{1 + {C_3}^2 + A^2{C_2}^2 - 2C_3\,(1+AC_2)\,\cos(\phi) + 2AC_2\,\cos(2\phi)}\right] \tag{6.3}$$

$$T_{drop}(\phi) = \left|\frac{\overline{\boldsymbol{E}}_{\boldsymbol{drop}}}{\overline{\boldsymbol{E}}_{\boldsymbol{in}}}\right|^2 = (1-\gamma)\left[\frac{(1-A^2)\left(1-{A_2}^2\right)\left(1-{A_3}^2\right)(1-\gamma)^2\tau^2}{1 + {C_3}^2 + A^2{C_2}^2 - 2C_3\,(1+AC_2)\,\cos(\phi) + 2AC_2\,\cos(2\phi)}\right] \tag{6.4}$$

$$\begin{cases} C_1 = A_2\,(1+AA_3)\,(1-\gamma)\,\tau \\ C_2 = A_3\,(1-\gamma)^2\tau^2 \\ C_3 = A_2\,(A+A_3)\,(1-\gamma)\,\tau \end{cases} \tag{6.5}$$

Regarding the FEM analysis, the dimensions, like the distance between waveguides, *d*, and the thickness, *w*, remain the same as in the previous add-drop RR models. The 2 ring-shaped waveguides have an equal radius *r* of 2,5 μm. The number of domains is the same, being the additional ring-shaped waveguide in the core domain, with the same real refractive index n_{core} of 3,2. Despite the geometry of this RR, the processing and the post-processing procedures are defined equally for this add-drop DRR.

Moreover, the transmittances of the output ports 2 and 4, the throughput and drop ports, respectively, of the add-drop DRR model are given by the Figure 6.2, being represented as function of the wavelength.

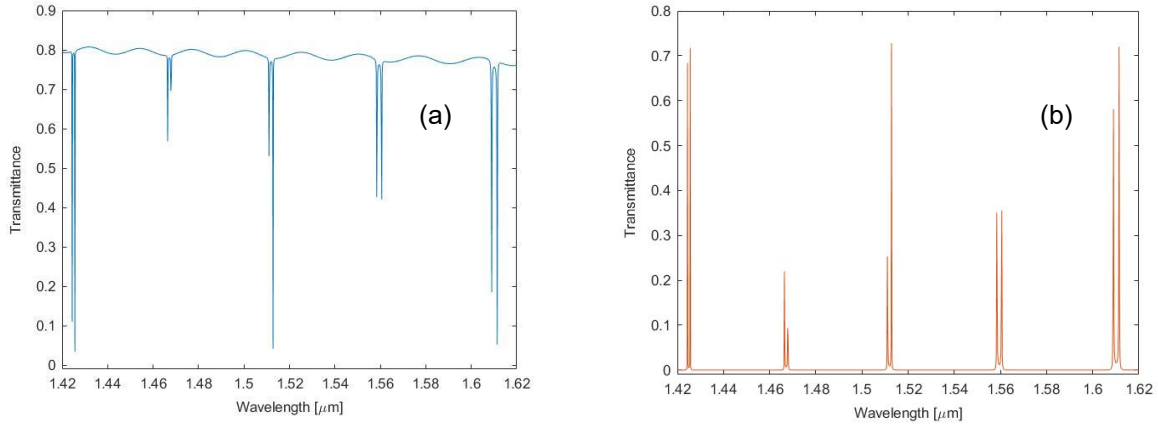

Figure 6.2 – Transmittances of the add-drop DRR: (a) – port 2, (b) – port 4.

Considering the transmittance results and the theoretical equations 6.1 and 6.2 for the add-drop DRR, it is now possible to determine the coupling and loss coefficients and obtain the analytical model of the add-drop DRR. To further simplify the analytical model, it is assumed that the coupling is lossless, that is, $(1 - \gamma)\ \tau = 1$, and the outer coupling coefficients are equal, $A = A_3$. As defined in chapter 5, the maximum and minimum of the cos ϕ allows the determination of the expressions for the maximums and minimums transmittances of the throughput and drop ports. Therefore, the maximum and minimum transmittances of the ports 2 and 4 can be defined by the equations 6.6, 6.7, 6.8 and 6.9.

$$T_{2_{max}} = (1-\gamma)\frac{\left(2A+A_2(1+A^2)\right)^2}{(1+2AA_2+A^2)^2} \tag{6.6}$$

$$T_{2_{min}} = (1-\gamma)\frac{\left(2A-A_2(1+A^2)\right)^2}{(1-2AA_2+A^2)^2} \tag{6.7}$$

$$T_{4_{max}} = (1-\gamma)\frac{(1-A^2)^2(1-{A_2}^2)}{(1-2AA_2+A^2)^2} \tag{6.8}$$

$$T_{4_{min}} = (1-\gamma)\frac{(1-A^2)^2(1-{A_2}^2)}{(1+2AA_2+A^2)^2} \tag{6.9}$$

The values of the T_{2min} and the T_{4max} are determined in the same manner as for the add-drop RR. The other 2 transmittances are calculated in a similar way, considering the interval of wavelengths for the mean values defined between the centre wavelengths of each 2 resonance peaks. The method for obtaining the effective refractive index and the additional phase shift is identical as for the add-drop RR, apart from using the central wavelengths between 2 resonance peaks. Moreover, it is only used 3 of the 4 equations for the calculus of the 3 coefficients, γ, A and A_2, being the equation 6.7, or 6.8, neglected.

Considering the Table 5.2 and the equations 5.5 and 5.6, n_{eff} ≈ 3,1150 and ϕ_0 ≈ -33,778 * 2π.

For the DRR, the mean transmittances of the ports 2 and 4 obtained are presented in the Table 6.1.

Table 6.1 – Maximum and minimum transmittances and means of the DRR.

Minimums of T_2	Maximums of T_4	Maximums of T_2	Minimums of T_4
0,11003	0,68401	0,80739	6,3095 x 10^{-7}
0,03404	0,71718		
0,56759	0,21975	0,80134	1,5959 x 10^{-7}
0,69605	0,09323		
0,53050	0,25353	0,79391	5,0350 x 10^{-8}
0,04181	0,72790		
0,42672	0,35081	0,78483	1,1656 x 10^{-6}
0,42051	0,35556		
0,18572	0,58174	0,76658	9,0806 x 10^{-6}
0,05220	0,72024		

$T_{2_{min}}$	$T_{4_{max}}$	$T_{2_{max}}$	$T_{4_{min}}$
0,30652	0,47037	0,79081	2,2174 x 10^{-6}

Taking into account the results from the Table 6.1 and knowing that the coupling coefficients and the insertion loss have a modulus less than 1, there are 2 possible solutions for both coupling coefficients, being $|A|$ ≈ 0,9610 and $|A_2|$ ≈ 0,9965 and a unique solution for the insertion loss, γ ≈ 0,2092.

Through the calculus of the coefficients and parameters for the application of the equations 6.1 and 6.2, the transmittances of the ports 2 and 4, for the analytical DRR, can be represented by the Figure 6.3.

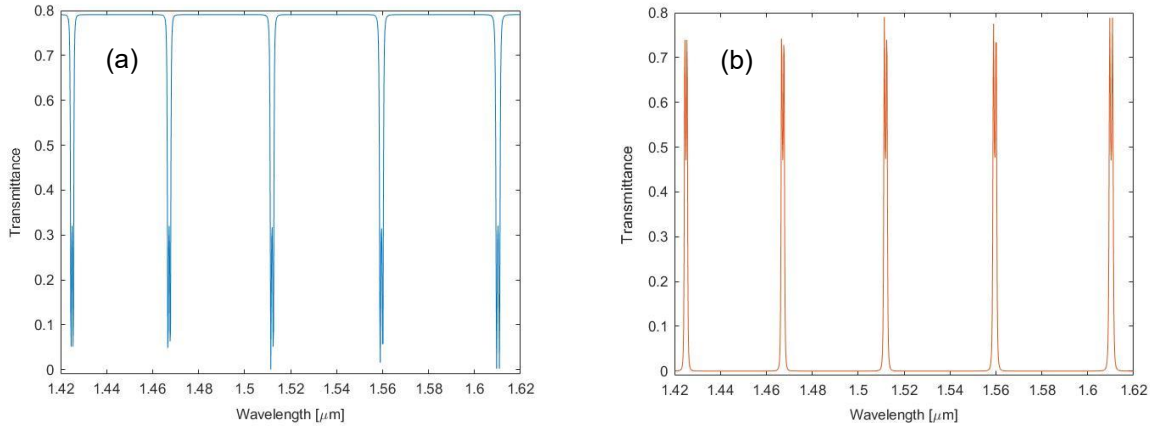

Figure 6.3 – Transmittances of the analytical add-drop DRR model: (a) – port 2, (b) – port 4.

In addition to considering the add-drop DRR with a radius, *r*, of 2,5 μm, for both ring-shaped waveguides, it is also examined another model with a smaller radius of 2,0 μm. All the other dimensions are kept the same as much as the physical domains defined and the post-processing procedures for the DRR.

The transmittances of the output ports 2 and 4, the throughput and drop ports, respectively, of the DRR with a radius of 2,0 μm are given by the Figure 6.4, being represented as function of the wavelength.

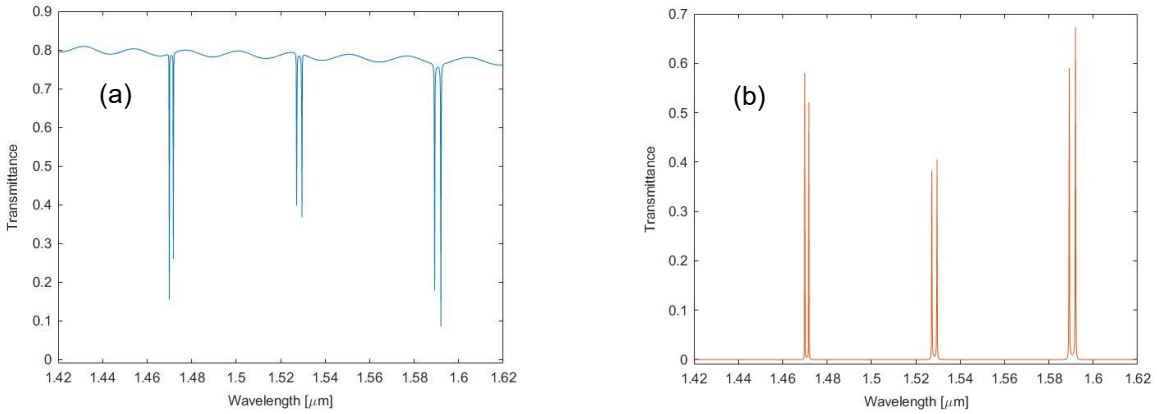

Figure 6.4 – Transmittances of the DRR with a radius of 2,0 μm: (a) – port 2, (b) – port 4.

The procedures to obtain the analytical model are the same as before with less resonance wavelengths. Considering the resonance wavelengths of the add-drop RR model with the same radius presented in Table 5.3, the refractive index, $n_{eff} \approx 3{,}1080$ and the additional phase, $\phi_0 \approx -25{,}554 * 2\pi$, are the same.

For this DRR, the mean transmittances of the ports 2 and 4 are presented in Table 6.2.

Table 6.2 – Maximum and minimum transmittances and means of the DRR – *r* = 2,0 μm.

Minimums of T_2	Maximums of T_4	Maximums of T_2	Minimums of T_4
0,11554	0,58013	0,79961	$1{,}6635 \times 10^{-7}$
0,26020	0,52101		
0,39749	0,38194	0,78867	$2{,}4305 \times 10^{-7}$
0,36797	0,40522		
0,17928	0,59043	0,78063	$6{,}9572 \times 10^{-8}$
0,08544	0,67261		

$T_{2_{min}}$	$T_{4_{max}}$	$T_{2_{max}}$	$T_{4_{min}}$
0,24096	0,52522	0,78964	$1{,}5966 \times 10^{-7}$

Taking into account the results from the Table 6.2 and knowing that the coupling coefficients and the insertion loss have a modulus less than 1, there are 2 possible solutions for both coupling coefficients, being $|A| \approx 0{,}9787$ and $|A_2| \approx 0{,}9991$ and a unique solution for the insertion loss, $\gamma \approx 0{,}2104$.

Through the calculus of the necessary coefficients and parameters, the transmittances of the ports 2 and 4 for the analytical model of the DRR with a radius of 2,0 μm can be represented by the Figure 6.5.

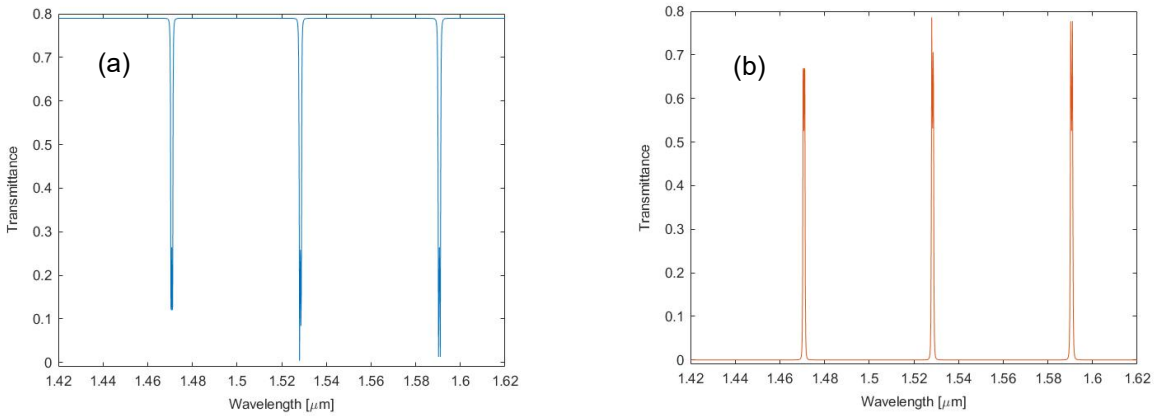

Figure 6.5 – Transmittances of the analytical DRR with a radius of 2,0 μm – (a): port 2, (b): port 4.

Furthermore, it is also examined another model with a different core material, being the radius of both ring-shaped waveguides defined as r = 2,5 μm. The chosen core material is the cadmium telluride, CdTe, modelled by Marple in 1964, with a real refractive index of 2,74 for the wavelength of 1,52 μm. The other parameters, such as the refractive index of the substrate, n_{sub}, are kept the same as much as the physical domains defined and the post-processing procedures for the add-drop double RR.

The transmittances of the output ports 2 and 4, the throughput and drop ports, respectively, of the DRR with a n_{core} = 2,74 are given by the Figure 6.6, being represented as function of the wavelength.

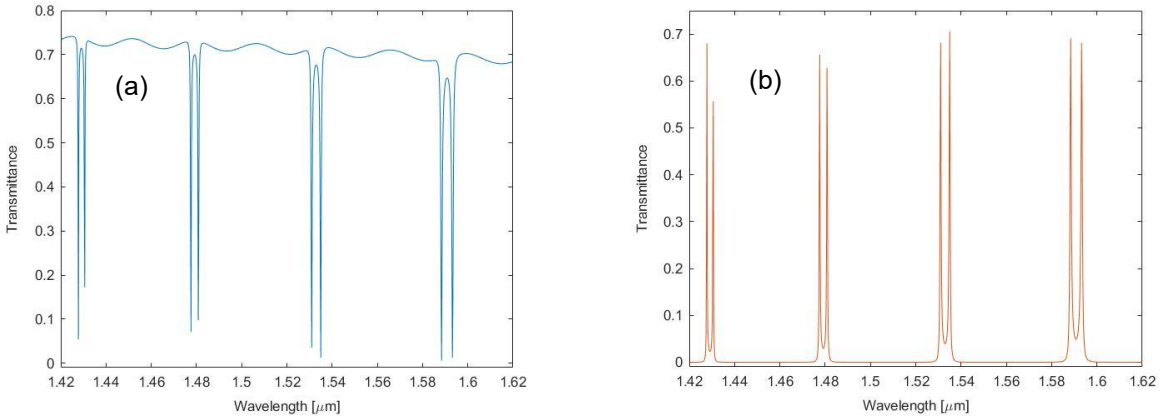

Figure 6.6 – Transmittances of the DRR with a n_{core} = 2,74: (a) – port 2, (b) – port 4.

The procedures to obtain the analytical model are the same as before with less resonance wavelengths. Considering the resonance wavelengths of the add-drop RR model with the same n_{core} presented in Table 5.7, the refractive index, $n_{eff} \approx 2{,}6863$ and the additional phase, $\phi_0 \approx -28{,}5285 * 2\pi$, are the same.

For this DRR, the mean transmittances of ports 2 and 4 obtained are presented in the Table 6.3.

Table 6.3 – Maximum and minimum transmittances and means of the DRR – n_{core} = 2,74.

Minimums of T_2	Maximums of T_4	Maximums of T_2	Minimums of T_4
0,05433	0,68022	0,73628	4,7473 x 10^{-6}
0,17182	0,55644		
0,07134	0,65575	0,72587	5,6908 x 10^{-6}
0,09794	0,62823		
0,03502	0,68116	0,71578	8,0112 x 10^{-6}
0,01229	0,70533		
0,00588	0,69092	0,70260	2,6049 x 10^{-5}
0,01221	0,68153		

$T_{2_{min}}$	$T_{4_{max}}$	$T_{2_{max}}$	$T_{4_{min}}$
0,05761	0,65995	0,72013	1,1125 x 10^{-5}

Taking into account the results from the Table 6.3 and knowing that the coupling coefficients and the insertion loss have a modulus less than 1, there are 2 possible solutions for both coupling coefficients, being $|A| \approx 0{,}9264$ and $|A_2| \approx 0{,}9947$ and a unique solution for the insertion loss, $\gamma \approx 0{,}2799$.

Through the calculus of the necessary coefficients and parameters, the transmittances of the ports 2 and 4 for the analytical model of the DRR with a n_{core} of 2,74 can be represented by the Figure 6.7.

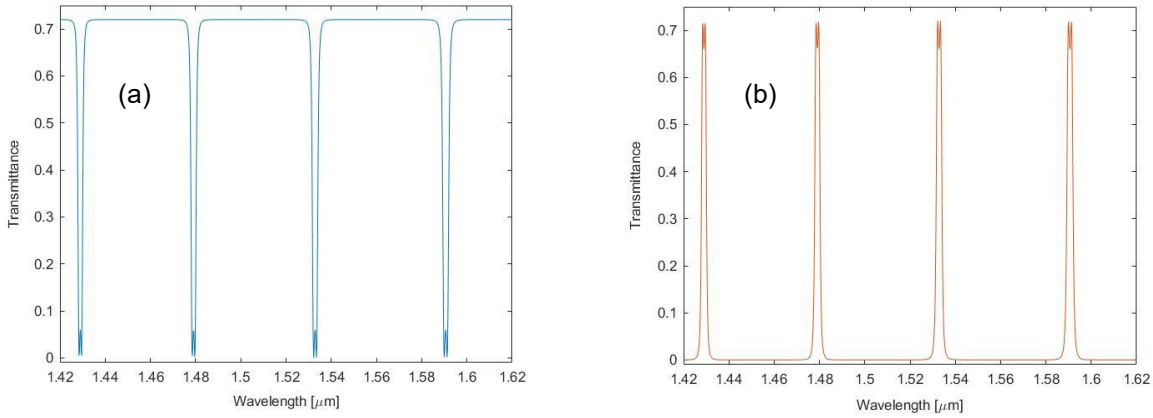

Figure 6.7 – Transmittances of the analytical DRR with a n_{core} of 2,74:
(a) – port 2, (b) – port 4.

For a better visualization of the differences between the simulated and analytical results, the transmittances of the ports 2 and 4, for the add-drop double RR models, are presented in Figure 6.8.

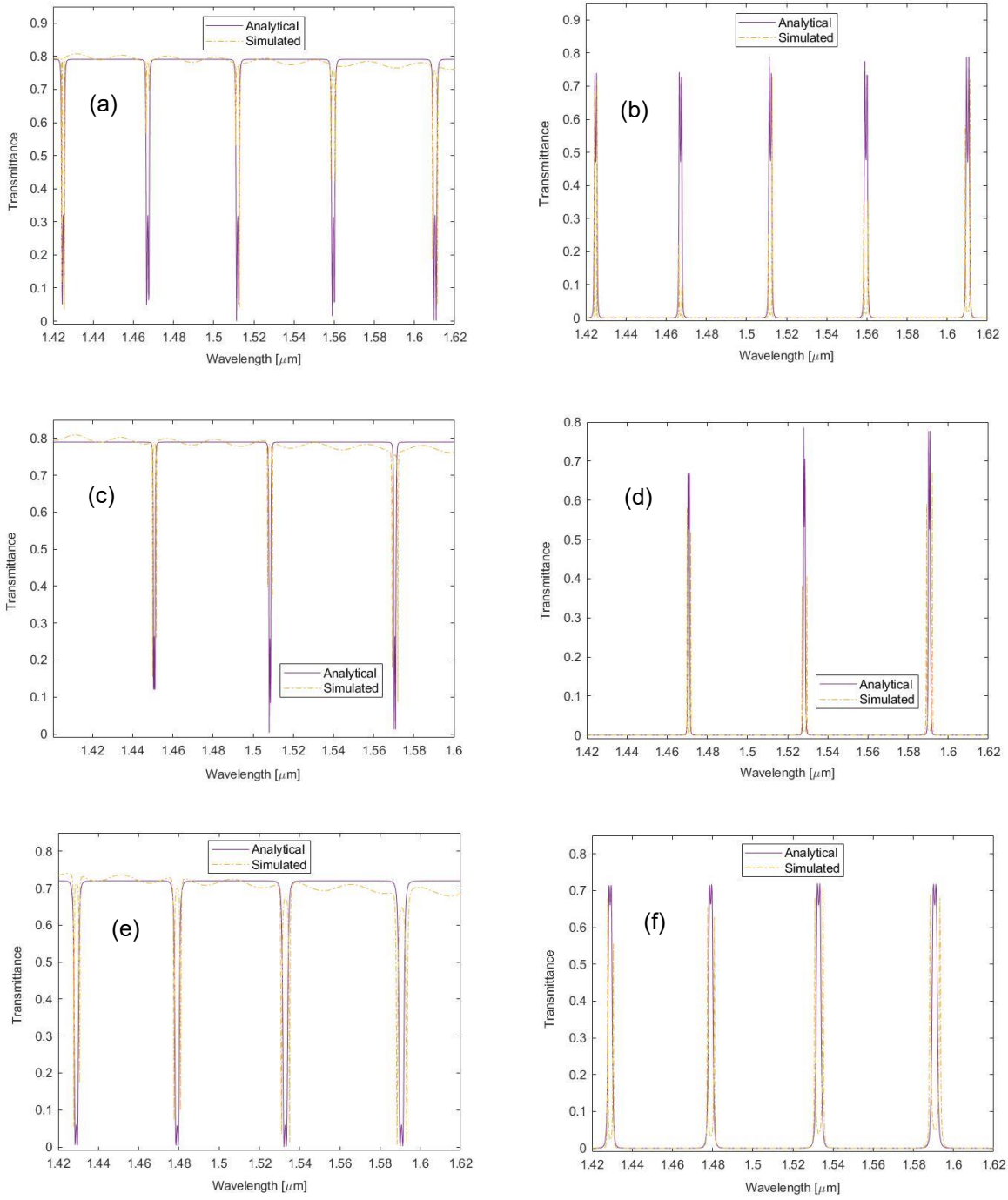

Figure 6.8 – Transmittances of the add-drop DRR models:

(a) – port 2 and (b) – port 4 : DRR model with a r = 2,5 μm and a n_{core} = 3,2;

(c) – port 2 and (d) – port 4 : DRR model with a radius of 2,0 μm;

(e) – port 2 and (f) – port 4 : DRR model with a n_{core} of 2,74.

Considering the results of the transmittances for each add-drop DRR model described, the main change, given the respective transmittances of the single RR models with the same parameters, is the number of resonance wavelengths, which doubles. This happens because these DRRs are over-coupled. In this scenario, resonance splitting occurs surrounding the central resonance wavelengths of the single RRs. This phenomenon is dependent on the coupling coefficients A and A_2, and it takes place when A_2 is lower than the critical coupling factor. The definition of the critical coupling factor is obtained in view of the equation 6.7 and the lossless coupling, being defined by the equation 6.10, for null transmittance.

$$A_{2_{crit}} = \frac{2A}{1+A^2} \tag{6.10}$$

For the critical coupling state, the FSR would be the same in each central resonance wavelength. Nevertheless, the FWHM, for each central resonance wavelength, would be distinct due to his dependence on the configuration of the RR. Hence, the quality factor and the finesse would also change.

The analytical resonance wavelengths are slightly different from the simulated ones. The maximum absolute error calculated between the resonance wavelengths obtained for both analytical and simulated models is of 2 nm, corresponding to 10 points difference in the parametric sweep, and the minimum absolute error is of 0,2 nm. The error rises with the increase of the resonance wavelengths for each model. This variation occurs because of the simplifications assumed for the analytical DRR models. The change of the values of transmittance in resonance between the results from the analytical and simulated models are due to the mean values assumed for the calculus of the coefficients.

Furthermore, the electric field profile of the DRR with a r = 2,5 μm and a n_{core} = 3,2 can be represented by the Figure 6.9, considering a condition in resonance and another at the maximum transmittance.

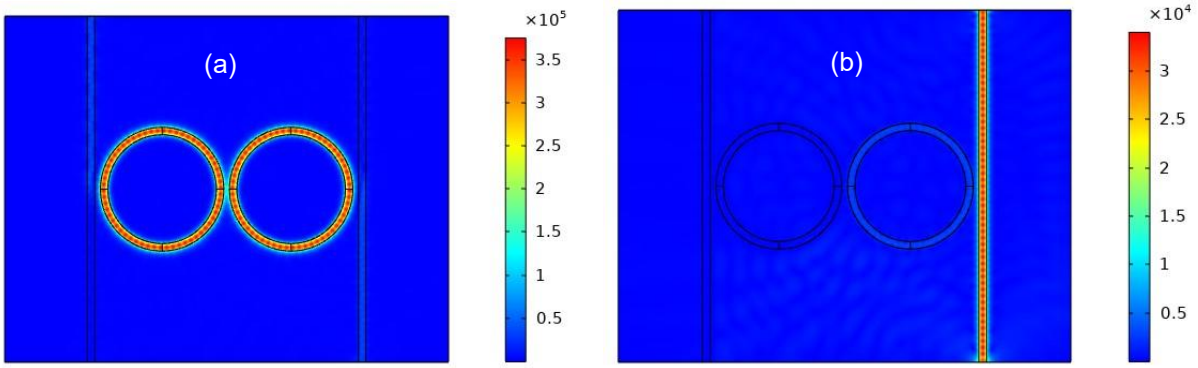

Figure 6.9 – Electric Field Profile in V/m of the DRR with a r of 2,5 μm and a n_{core} of 3,2:

(a) - In resonance, λ = 1,4256 μm;

(b) - At the maximum transmittance of port 2, λ = 1,4318 μm.

Besides, in this appendix A, extra transmittance results for other models of the add-drop DRR, with distinct radii for the ring-shaped waveguides, are presented, as well as for analytical DRR models with equal coupling coefficients, A = A_2. In this case, the equations 6.6 and 6.9 are the only considered.

7

Add-drop Triple RR: Description and Analysis

The add-drop triple RR, TRR, is the third and last optical system that is studied taking into account the analytical analysis and the FEM. This serially coupled RR model has two more ring-shaped waveguides than the first add-drop RR model and its configuration can be represented by the Figure 7.1.

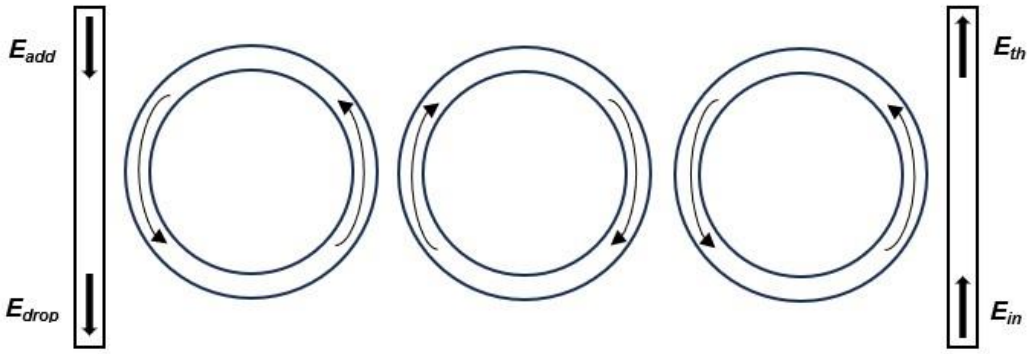

Figure 7.1 – Add-drop Triple RR.

The analytical analysis of the add-drop TRR is done considering that the input power is equal to the output power, that is, the coupling is lossless and the light inside the waveguides are partially transmitted in the coupling region. Regarding this simplification and taking into account the signal flow graph method used for the add-drop double RR to describe the relation between the output and input fields, the ratio between the drop field, $\overline{E}_{drop}$, and the input field, $\overline{E}_{in}$, and the ratio between the throughput field, $\overline{E}_{th}$, and the input field, $\overline{E}_{in}$, for the add-drop TRR model, are given by the equations 7.1 and 7.2.

$$\frac{\overline{E}_{th}}{\overline{E}_{in}} = \sqrt{1-\gamma}\left[\frac{A-(A_2+AA_2A_3+AA_3A_4)(1-\gamma)\tau\, e^{-j\phi}+(A_3+A_2A_3A_4+AA_2A_4)(1-\gamma)^2\tau^2\, e^{-j2\phi}+A_4(1-\gamma)^3\tau^3\, e^{-j3\phi}}{1-(AA_2+A_2A_3+A_3A_4)(1-\gamma)\tau\, e^{-j\phi}+(AA_3+A_2A_4+AA_2A_3A_4)(1-\gamma)^2\tau^2\, e^{-j2\phi}+AA_4(1-\gamma)^3\tau^3\, e^{-j3\phi}}\right] \quad (7.1)$$

$$\frac{\overline{E}_{drop}}{\overline{E}_{in}} = \sqrt{1-\gamma}\left[\frac{BB_2B_3B_4\left[(1-\gamma)\tau\, e^{-j\phi}\right]^{3/2}}{1-(AA_2+A_2A_3+A_3A_4)(1-\gamma)\tau\, e^{-j\phi}+(AA_3+A_2A_4+AA_2A_3A_4)(1-\gamma)^2\tau^2\, e^{-j2\phi}+AA_4(1-\gamma)^3\tau^3\, e^{-j3\phi}}\right] \quad (7.2)$$

For the add-drop TRR analytical model, it is considered that the intensity loss coefficients are equal for all couplers, $\gamma = \gamma_2 = \gamma_3 = \gamma_4$. The real coupling coefficients are represented as A, A_2, A_3, A_4 and B, B_2, B_3 and B_4, which follow the same relation for each coupling defined by equation 3.3. The transmission factor τ and the optical phase ϕ are defined in the same way as presented in chapter 3.

Given the equations 7.1 and 7.2, the transmittances for the throughput and drop ports are given by the equations 7.4 and 7.5, being C_1, C_2, C_3, C_4 and C_5 real coefficients defined in equation 7.3.

$$\begin{cases} C_1 = (A_2 + AA_2A_3 + AA_3A_4)(1-\gamma)\tau \\ C_2 = (A_3 + A_2A_3A_4 + AA_2A_4)(1-\gamma)^2\tau^2 \\ C_3 = A_4(1-\gamma)^3\tau^3 \\ C_4 = (AA_2 + A_2A_3 + A_3A_4)(1-\gamma)\tau \\ C_5 = (AA_3 + A_2A_4 + AA_2A_3A_4)(1-\gamma)^2\tau^2 \end{cases} \quad (7.3)$$

$$T_{th}(\phi) = \left|\frac{\overline{E}_{th}}{\overline{E}_{in}}\right|^2 = (1-\gamma)\left[\frac{A^2+C_1{}^2+C_2{}^2+C_3{}^2-2(AC_1+C_1C_2+C_2C_3)\cos(\phi)+2(AC_2+C_1C_3)\cos(2\phi)-2AC_3\cos(3\phi)}{1+C_4{}^2+C_5{}^2+A^2C_3{}^2-2(C_4+AC_3C_5+C_4C_5)\cos(\phi)+2(AC_3C_4+C_5)\cos(2\phi)-2AC_3\cos(3\phi)}\right] \quad (7.4)$$

$$T_{drop}(\phi) = \left|\frac{\overline{E}_{drop}}{\overline{E}_{in}}\right|^2 = (1-\gamma)\left[\frac{(1-A^2)(1-A_2{}^2)(1-A_3{}^2)(1-A_4{}^2)(1-\gamma)^3\tau^3}{1+C_4{}^2+C_5{}^2+A^2C_3{}^2-2(C_4+AC_3C_5+C_4C_5)\cos(\phi)+2(AC_3C_4+C_5)\cos(2\phi)-2AC_3\cos(3\phi)}\right] \quad (7.5)$$

Regarding the FEM analysis, the dimensions, like the distance between waveguides, *d*, and the thickness, *w*, remain the same as in the previous add-drop RR models. The 3 ring-shaped waveguides have an equal radius *r* of 2,5 μm. The number of domains is the same, being the additional ring-shaped waveguides in the core domain, with the same real refractive index n_{core} of 3,2. Despite the geometry of this RR, the processing and the post-processing procedures are defined equally for this add-drop TRR.

Moreover, the transmittances of the output ports 2 and 3, the throughput and drop ports, respectively, of this add-drop TRR model are given by the Figure 7.2, being represented as function of the wavelength.

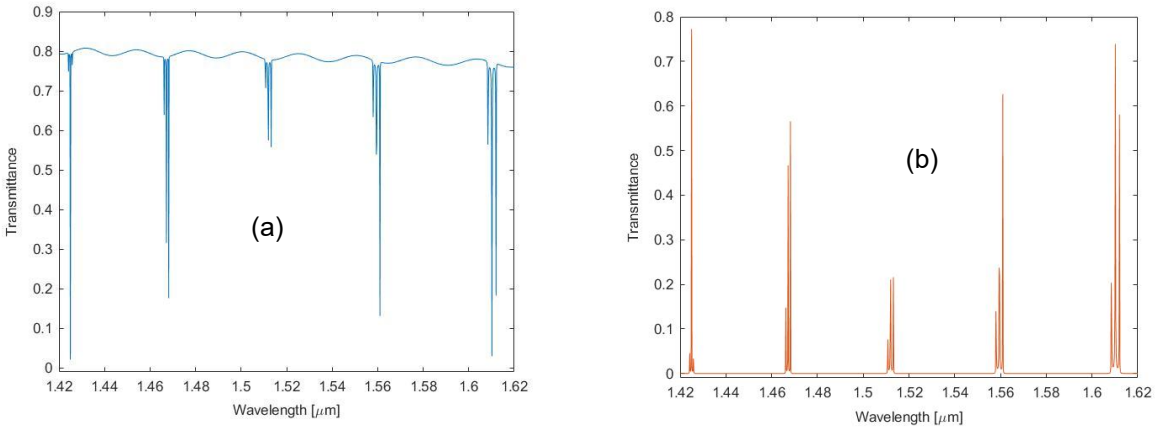

Figure 7.2 – Transmittances of the add-drop TRR: (a) – port 2, (b) – port 3.

Given the transmittance results and the theoretical equations 7.1 and 7.2 for the add-drop TRR, it is now possible to determine the coupling and loss coefficients and obtain the analytical model. To further simplify the analytical model, it is assumed that $(1 - \gamma)\ \tau = 1$, accordingly to lossless coupling. Likewise, the outer and internal coupling coefficients are equal, $A = A_4 = A_2 = A_3$. As defined in chapter 5 for the add-drop RR, the maximum and minimum of the cos ϕ allows the determination of the expressions for the maximums and minimums transmittances of the throughput and drop ports. Therefore, the minimum transmittance of the port 3 and the maximum transmittance of the port 2 can be defined by the equations 7.6 and 7.7, being T_{2min} equal to zero and T_{3max} equal to one, with these simplifications.

$$T_{2_{max}} = (1-\gamma)\frac{16\left(A+A^3\right)^2}{(1+A^4+6A^2)^2} \tag{7.6}$$

$$T_{3_{min}} = (1-\gamma)\frac{(1-A^2)^4}{(1+A^4+6A^2)^2} \tag{7.7}$$

These 2 mean transmittances values are calculated in a similar way as before for the other RR models, considering the interval of wavelengths for the mean values defined between the central wavelengths of each 3 resonance peaks. The method for obtaining the effective refractive index, n_{eff}, and the additional phase shift is identical, apart from using the central wavelengths of each 3 resonance peaks. Hence and considering the Table 5.2 and the equations 5.5 and 5.6, $n_{eff} \approx 3{,}1150$ and $\phi_0 \approx -33{,}778 * 2\pi$.

The maximums of T_2, the minimums of T_3, and the means obtained are presented in the Table 7.1.

Table 7.1 – Maximum and minimum transmittances and means of the TRR.

Maximums of T_2	0,80764	0,80106	0,79372	0,78537	0,76721
Minimums of T_3	7,136 x 10^{-9}	6,420 x 10^{-9}	5,526 x 10^{-8}	6,357 x 10^{-9}	6,770 x 10^{-7}

$T_{2_{max}}$	0,79100	$T_{3_{min}}$	1,504 x 10^{-7}

Considering the results from the Table 7.1 and the theoretical equations 7.6 and 7.7, there is a unique solution for the coupling coefficient modulus and the loss, being $|A| \approx 0{,}9709$ and $\gamma \approx 0{,}2090$.

Through the calculus of the coefficients and parameters for the application of the equations 7.4 and 7.5, the transmittances of the ports 2 and 3 for the analytical TRR can be represented by the Figure 7.3.

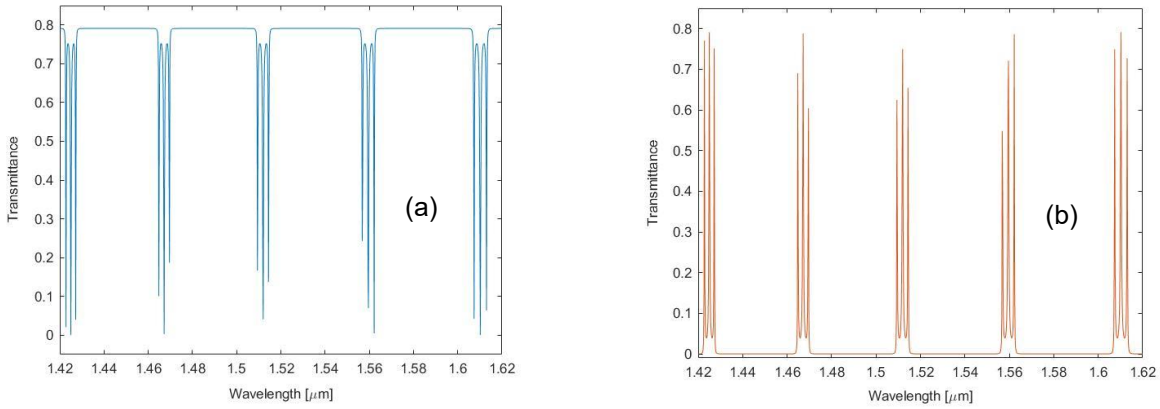

Figure 7.3 – Transmittances of the analytical add-drop TRR model: (a) – port 2, (b) – port 3.

In addition to considering the add-drop TRR with a radius, *r*, of 2,5 μm, for the 3 ring-shaped waveguides, it is also examined another TRR with a smaller radius of 2,0 μm. All the other dimensions are kept the same as much as the physical domains defined and the post-processing procedures for the TRR.

The transmittances of the output ports 2 and 3, the throughput and drop ports, respectively, of the TRR with a radius of 2,0 μm are given by the Figure 7.4, being represented as function of the wavelength.

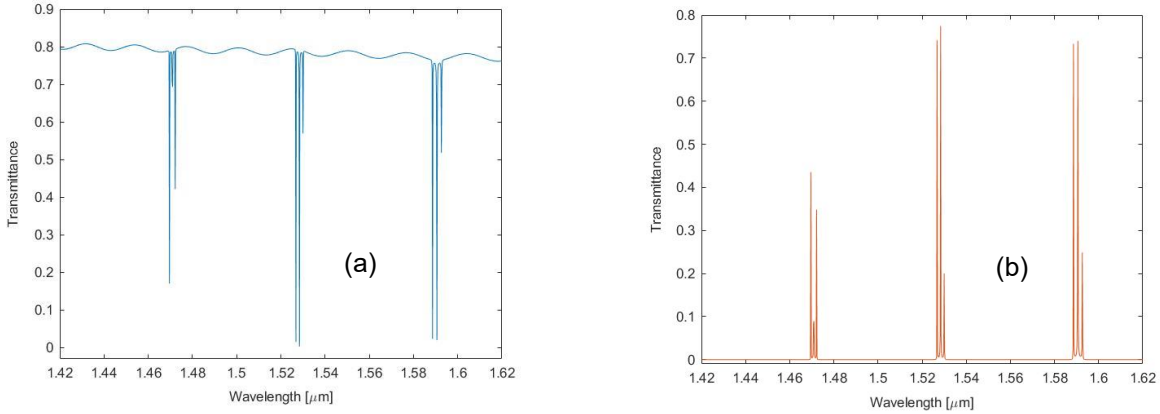

Figure 7.4 – Transmittances of the TRR with a radius of 2,0 μm: (a) – port 2, (b) – port 3.

The procedures to obtain the analytical model are the same as before with less resonance wavelengths. Considering the resonance wavelengths of the add-drop RR model with the same radius presented in Table 5.3, the refractive index, n_{eff} ≈ 3,1080 and the additional phase, ϕ_0 ≈ -25,554 * 2π , are the same.

The maximums of T_2, the minimums of T_3, and the means obtained are presented in the Table 7.2.

Table 7.2 – Maximum and minimum transmittances and means of the TRR – *r* = 2,0 μm.

Maximums of T_2	0,80032	0,78924	0,78154	$T_{2_{max}}$	0,79037
Minimums of T_3	4,780 x 10^{-9}	2,529 x 10^{-8}	1,719 x 10^{-7}	$T_{3_{min}}$	6,733 x 10^{-8}

Considering the results from the Table 7.2 and the theoretical equations 7.6 and 7.7, there is a unique solution for the coupling coefficient modulus and the loss, being |A| ≈ 0,9761 and γ ≈ 0,2096.

Through the calculus of the necessary coefficients and parameters, the transmittances of the ports 2 and 3 for the analytical model of the TRR with a radius of 2,0 μm can be represented by the Figure 7.5.

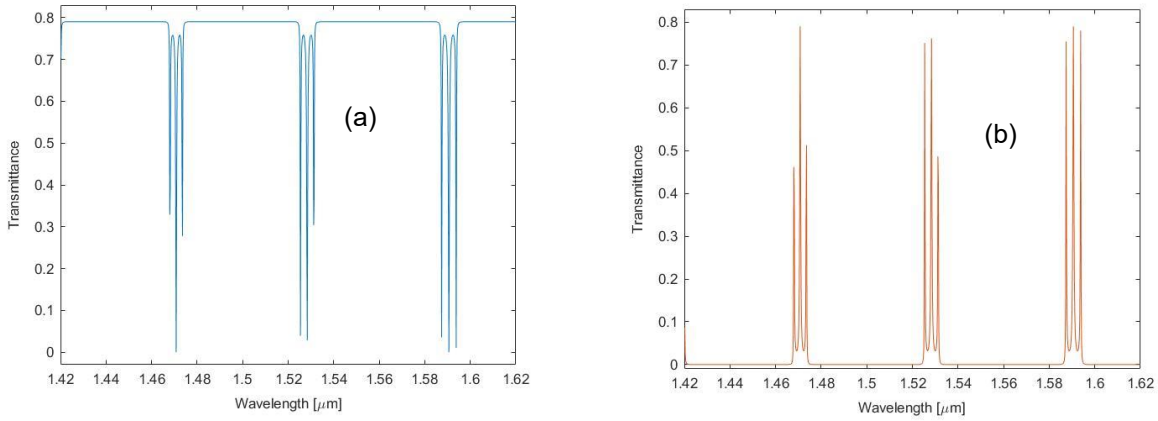

Figure 7.5 – Transmittances of the analytical TRR with a radius of 2,0 μm – (a): port 2, (b): port 3.

Furthermore, it is also examined another TRR model with a different core material, being the radius of the 3 ring-shaped waveguides defined as *r* = 2,5 μm. The chosen core material is the cadmium telluride, CdTe, modelled by Marple in 1964, with a real refractive index of 2,74 for the wavelength of 1,52 μm. The other parameters, such as the refractive index of the substrate, n_{sub}, are kept the same as much as the physical domains defined and the post-processing procedures for the add-drop triple RR.

The transmittances of the output ports 2 and 3, the throughput and drop ports, respectively, of the TRR with a n_{core} = 2,74 are given by the Figure 7.6, being represented as function of the wavelength.

The procedures to obtain the analytical model are the same with more resonance wavelengths. Considering the resonance wavelengths of the add-drop RR model with the same n_{core} presented in Table 5.7, the refractive index, n_{eff} ≈ 2,6863 and the additional phase, ϕ_0 ≈ -28,5285 * 2π , are the same.

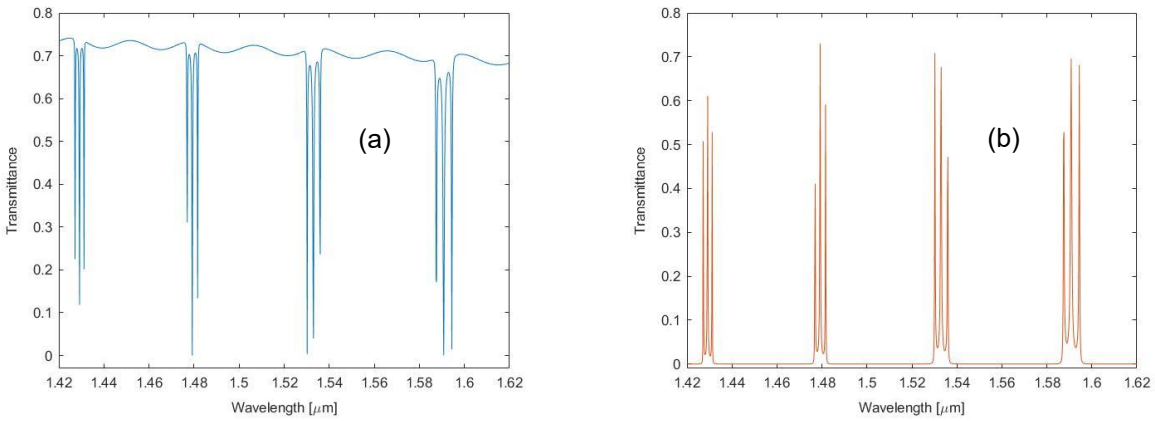

Figure 7.6 – Transmittances of the TRR with a n_{core} = 2,74: (a) – port 2, (b) – port 3.

The maximums of T_2, the minimums of T_3, and the means obtained are presented in the Table 7.3.

Table 7.3 – Maximum and minimum transmittances and means of the TRR – n_{core} = 2,74.

Maximums of T_2	0,73561	0,72730	0,71627	0,70341
Minimums of T_3	4,637 x 10^{-8}	8,922 x 10^{-7}	1,851 x 10^{-6}	2,232 x 10^{-6}

$T_{2_{max}}$	0,72065	$T_{3_{min}}$	1,2555 x 10^{-6}

Considering the results from the Table 7.3 and the theoretical equations 7.6 and 7.7, there is a unique solution for coupling coefficient modulus and the loss, being $|A| \approx 0{,}9499$ and $\gamma \approx 0{,}2794$.

Through the calculus of the necessary coefficients and parameters, the transmittances of the ports 2 and 3 for the analytical model of the TRR with a n_{core} of 2,74 can be represented by the Figure 7.7.

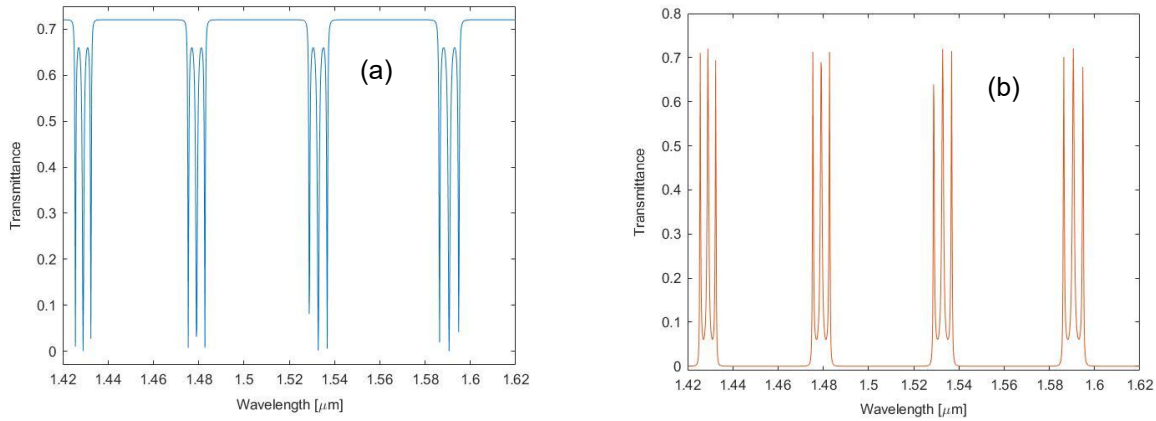

Figure 7.7 – Transmittances of the analytical TRR with a n_{core} of 2,74:
(a) – port 2, (b) – port 3.

For a better visualization of the similarities between the simulated and analytical results, the transmittances of the ports 2 and 3, for the add-drop triple RR models, are presented in Figure 7.8.

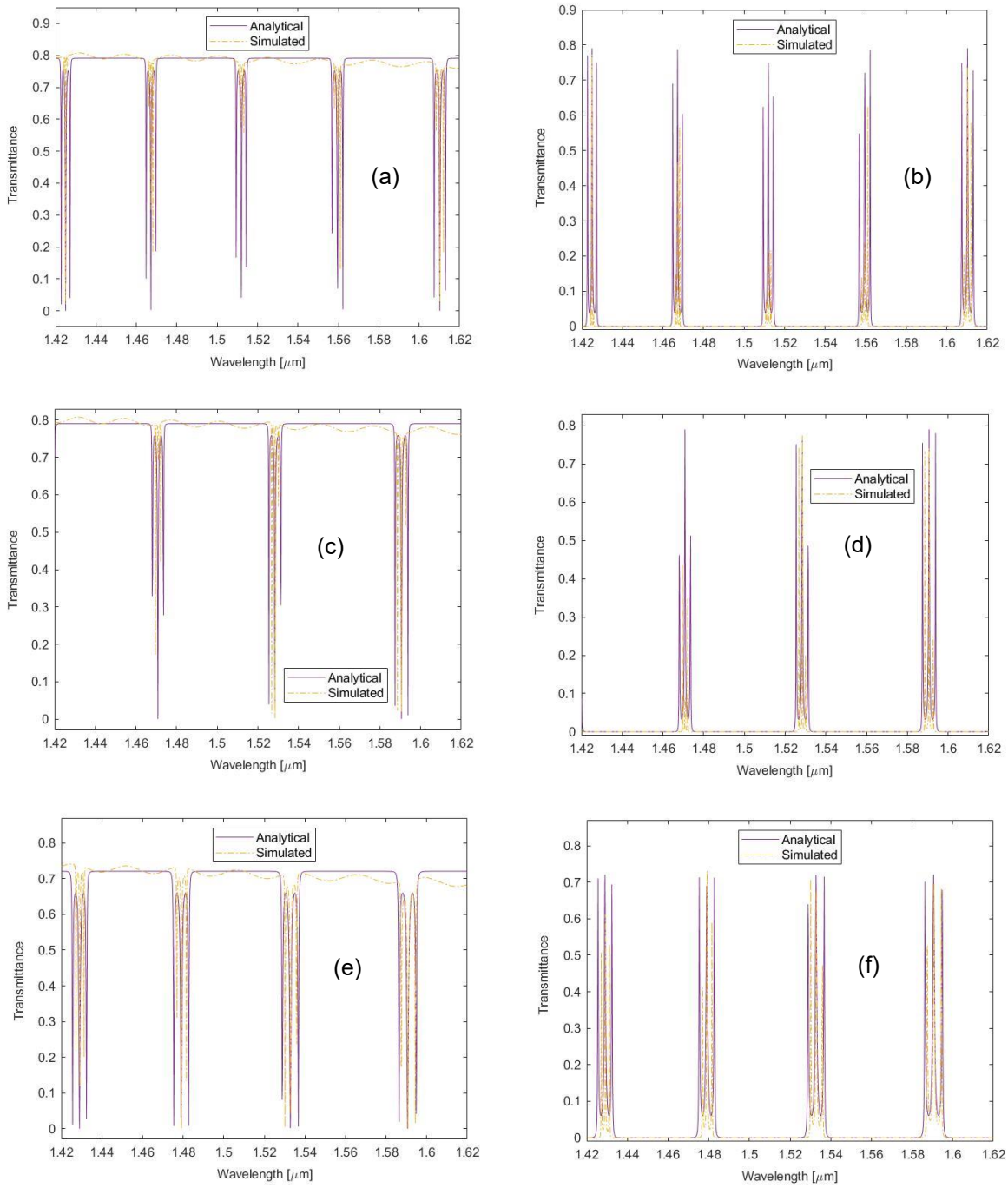

Figure 7.8 – Transmittances of the add-drop TRR models:

(a) – port 2 and (b) – port 3 : TRR model with a r = 2,5 μm and a n_{core} = 3,2;

(c) – port 2 and (d) – port 3 : TRR model with a radius of 2,0 μm;

(e) – port 2 and (f) – port 3 : TRR model with a n_{core} of 2,74.

Furthermore, the electric field profile of the TRR with a r = 2,5 μm and a n_{core} = 3,2 can be represented by the Figure 7.9, considering a condition in resonance and another at a high transmittance.

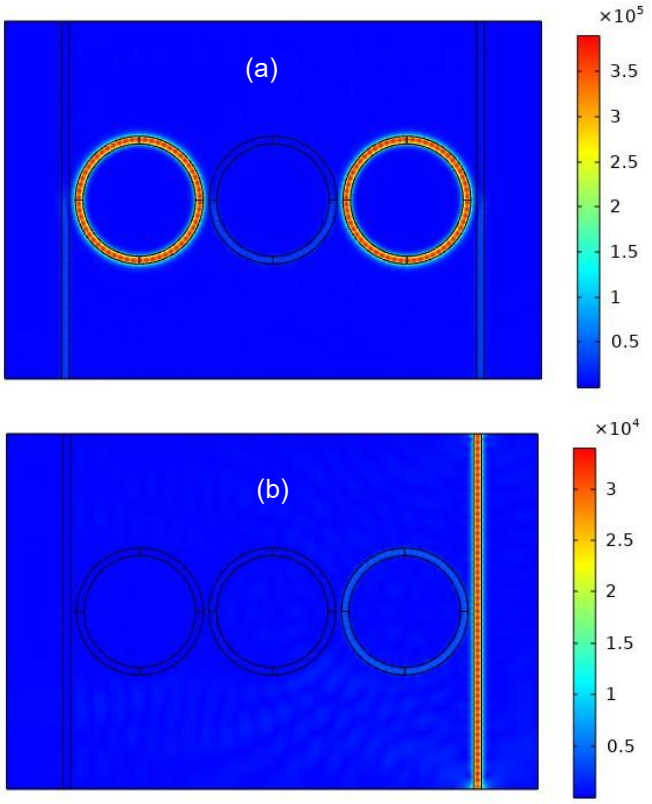

Figure 7.9 – Electric Field Profile in V/m of the TRR with a *r* of 2,5 μm and a n_{core} of 3,2:

(a) - In resonance, $\lambda = 1{,}4250$ μm;

(b) - At a high transmittance of port 2, $\lambda = 1{,}4300$ μm.

Considering the results of the transmittances for each TRR described, the main change, given the respective transmittances of the single RRs with the same parameters, is the number of resonance wavelengths, which is the triple. This happens because these TRRs are over-coupled. In this scenario, resonance splitting also occurs surrounding the central resonance wavelengths of the single RRs. In comparison with the DRRs, the resonance also happens in the central wavelengths of the splitting.

Without the resonance splitting, the FSR would be the equal in each central resonance wavelength. Nevertheless, the FWHM, for each central resonance wavelength, would be distinct due to his dependence on the configuration of the RR. Hence, the quality factor and the finesse would also change.

The central analytical resonance wavelengths are approximately equal to the simulated ones, in which the absolute error is, at maximum, 0,2 nm. Considering the other resonance wavelengths, the absolute error increases, being 1,6 nm at maximum and 0,4 nm at minimum. However, for the TRR models, the absolute error drops with the increase in the resonance wavelength. The change of the values of transmittance in resonance between the results from the analytical and simulated models are due to the mean values assumed for the calculus of the coefficients and the approximate solutions obtained.

8

Conclusion

In this research, the description, and the analysis of WDM systems is developed considering 3 main configurations of ring resonators considering the theoretical basis presented in the state-of-the-art and used in *MATLAB* and the finite element method applied in the *COMSOL Multiphysics* tool.

To do the research on WDM systems, the wave theory is introduced regarding the propagation of light waves, taking into account the characteristics of the medium and the relationship between the fields. These fields are expressed as phasors for plane waves and the theoretical equations are established. Furthermore, the fundamental parameters and sections of planar optical waveguides are also defined. In this waveguides, the conditions for light propagation are presented, namely the equation that specifies the propagation constants of the modes, in which exists transmission of light. A 2D waveguide example, known as slab waveguide, is described, having only two fundamental modes, the transversal electric and transversal magnetic modes. For examining more complex two-dimensional waveguide structures, the finite element method is a more accurate method. Moreover, the effective index method allows the reduction of three-dimensional waveguides onto 2D structures. Besides these methods and for ring resonators, the **coupling** of two or more waveguides are crucial.

The 3 configurations of the ring resonators examined have 2 bus waveguides and an increasing number of ring-shaped waveguides, being one for the first, 2 for the second and three for the last topology. In the state-of-the-art, the theoretical basis of ring resonators and the respective parameters are stated. The signal flow graph along with the Mason's rule is used to obtain the analytical equations for the ratio between the output and input fields, required for the determination of the analytical models of the ring resonators. To compare the output response of the simulated and analytical models for the ring resonators with distinct radii and materials, the transmittances of the 2 output ports are determined.

Considering the results of the ring resonators models, the transmittance, except for the resonance peaks, is identical for the 3 topologies with the same dimensions and materials. The main difference between ring resonators topologies with the same parameters is the number of resonance wavelengths, that is higher due to the increase in the number of ring-shaped waveguides. The decrease in the radii of the ring-shaped waveguides also changes the number of resonance wavelengths for the 3 topologies, with the FSR increase. For the models with different core materials, the higher transmittances decrease with lower core refractive indexes and the resonance width increases. The change of the values of transmittance in resonance between the results from the analytical and simulated models are due to the mean values assumed for the calculus of the coefficients.

These results show that the theoretical methods are an effective tool to verify the output responses of the RR models. Also, the number of waveguides, the core materials and the radii *r* of RR are parameters which allow the tuning of the output response needed for WDM applications. Furthermore, the RR devices can work as wavelength multiplexers, with the transmission of the resonance wavelengths.

For future research within these WDM analyses for ring resonators, the width of the straight waveguides or the distance between waveguides can be modified as well as the optical bands chosen for the sweep.

References

[1] O.E. Delange, Wideband optical communication systems, Part II – Frequency division multiplexing, *Proc IEEE*, vol.58, p.1683, October 1970.

[2] Ishio, H., Minowa, J., and K. Nosu, Review and Status of Wavelength-Division-Multiplexing Technology and Its Application, *Journal of Lightwave Technology*, vol. Lt-2, No.4, August 1984.

[3] Keiser, G. E., A Review of WDM Technology and Applications, *Optical Fiber Technology* **5**, 3-39, 1999.

[4] Smit, M. K. and C. Van Dam, "PHASAR-based WDM devices: Principles, design and applications, *IEEE J.Selected Topcis Quantum Electronics,* vol.2, 236, 1996.

[5] Fonjallaz, P.- Y., H. G. Limberger, and R. P. Salanthé, Bragg gratings with efficient and wavelength-selective fiber out-coupling, *J. Lightwave Technol.*, vol.15, 371, 1997.

[6] Okamoto, K., Fundamentals of Optical Waveguides, *Elsevier*, 2021.

[7] Stratton, J. A, Electromagnetic Theory, *New York: McGraw-Hill*, 1941.

[8] Born, M. and E. Wolf, Principles of optics: electromagnetic theory of propagation, interference and diffraction of light, *Elsevier*, 2013.

[9] Marcuse, D., Theory of Dielectric Optical Waveguides, *New York: Academic Press*, 1974.

[10] https://www.intechopen.com/chapters/61838, visited in 2023.

[11] Marcatili, E. A. J., Dielectric rectangular waveguide and directional coupler for integrated optics, *Bell Syst, Tech, J.*, 48:2071-2102, 1969.

[12] Kumar, A., K. Thyagarajan and A. K. Ghatak, Analysis of rectangular-core dielectric waveguides-An accurate perturbation approach, *Opt Lett*, 8:63-65, 1983.

[13] Huang, W. P., Coupled-mode theory for optical waveguides: an overview, *J. Opt. Soc. Am. A,* Vol.11, No.3, March 1994.

[14] Takato, N., M. Kawachi, M. Nakahara, and T. Miyashita, Silica-based single-mode guided-wave devices, *Integrated Optics Optoelectronics*, SPIE 1177:92-100, 1989.

[15] Stokes, L. F., M. Chorodow, and H. J. Shaw, All-single-mode fiber resonator, *Opt. Lett*, 7:288-290, 1982.

[16] https://www.comsol.com/model/optical-ring-resonator-notch-filter-22221, accessed in 2022.

[17] Heebner, J. E., V. Wong, A. Schweinsberg, R. W. Boyd, and D. J. Jackson, Optical Transmission Characteristics of Fiber Ring Resonators, *IEEE Journal of Quantum Electronics,* vol.40, no.6, June 2004.

[18] Yariv, A., Critical Coupling and Its Control in Optical Waveguide - Ring Resonator Systems, *IEEE Photonics Technology Letters,* vol.14, no.4, April 2002.

[19] Van, V., T. A. Ibrahim, K. Ritter, P. P. Absil, F. G. Johnson, R. Grover, J. Goldhar, and P.- T. Ho, All-optical nonlinear switching in GaAs-Al-GaAs microring resonators, *IEEE Photon. Technol. Lett.,* vol.14, pp.74-77, January 2002.

[20] Heebner, J. E., and R. W. Boyd, Enhanced all-optical switching by use of a nonlinear fiber ring resonator, *Opt. Lett.,* vol.24, pp.847-849, 1999.

[21] Boyd, R. W., and J. E. Heebner, Sensitive disk-resonator photonic biosensor, *Appl. Opt.,* vol.40, pp.5742-5747, 2001.

[22] McCall, S. L., A. F. J. Levi, R. E. Slusher, S. J. Pearton, and R. A. Logan, Whispering-gallery mode microdisk lasers, *Appl. Phys. Lett.,* vol.60, pp. 289-291, 1992.

[23] Little, B. E., S. T. Chu, A. Haus, J. Foresi, and J. -P. Laine, Microring resonator channel dropping filters, *J. Lightwave Technol.,* vol.15, pp.998-1005, April 1997.

[24] Afroozeh, A., I. S. Amiri, K. Chaudhary, J. Ali, and P. P. Yupapin, Analysis of Optical Ring Resonator, *Advances in Laser and Optics Research*, vol. 11, ch.6, 2015.

[25] Rabus, D. G., Ring Resonators: Theory and Modeling, *Integrated Ring Resonators,* 2007.

[26] Weber, H., and R. Ulrich, A Thin-Film Ring Laser, *Applied Physics Letters,* pp.38-40, 1971.

[27] Ulrich, R., and H. Weber, Unidirectional Thin-Film Ring Laser, *Applied Physics Letters,* 1972.

[28] Ulrich, R., and H. Weber, Solution-deposited thin films as passive and active light-guides, *Applied Optics,* pp.288-290, 1972.

[29] Haavisto, J., and G. Pajer, Resonance effects in low-loss ring waveguides, *Optics Letters,* 1982.

[30] Oda, K., N. Takato, and H. Toba, A wide-FSR waveguide double ring resonator for optical FDM transmission systems, *Journal of Lightwave Technology*, 1991.

[31] Wang, W., et al., New integrated optical ring resonator in glass, *Electronic Letters,* 1992.

[32] Chu, S.T, et al., Cascaded microring resonators for crosstalk reduction and spectrum cleanup in add-drop filters, *IEEE Photonics Technology Letters,* p.1423-1425, 1999.

[33] Rabiei, P., and W.H. Steier, Micro-ring resonators using polymer materials, *IEEE,* 2001.

[34] Rabiei, P. et al., Polymer micro-ring resonators filters and modulators, *Journal of Lightwave Technology,* 2002.

[35] Hryniewicz, J., et al., Microring resonator notch filters, *IEEE,* 2000.

[36] Wu, D., Y. Wu, Y. Wang, J. An and X. Hu, Reconfigurable optical add-drop multiplexer based on thermally tunable micro-ring resonators, *Optics Communications 367,* 44-49*,* 2016.

[37] Parandin, F. and N. Bagheri, Design of a 2 x 1 multiplexer with a ring resonator based on 2D photonic crystals, *Optics 11,* 2023.

[38] Jile, H., Application of nonlinear ring resonators for realizing all-optical digital multiplexers, *Photonics and Nanostructures – Fundamentals and Applications 45,* 2021.

[39] Jagota, V., A. P. S. Sethi, and K. Kumar, Finite Element Method: An Overview, *Walailak Journal,* 2013.

[40] Clough, R. W., The finite element method in a plane stress analysis, *Proceedings of the 2nd ASCE Conference on Electronic Computation,* 1960.

[41] Courant, R., Variational methods for the solutions of equilibrium and vibrations, *Bull. Am. Math, Soc.,* **49**, 1-23, 1943.

[42] Hrenikoff, A., Solution of problems in elasticity by the framework method, *J. Appl. Mech*, 1941.

[43] Zienkiewicz, C., and Y. K. Cheung, Finite elements in the solution of field problems, *Engineer,* **220**, 507-10, 1965.

[44] https://www.comsol.com/multiphysics/finite-element-method, visited in 2023.

[45] https://www.jousefmurad.com/fem/the-finite-element-method-beginners-guide, accessed in 2023.

[46] https://doc.comsol.com/5.4/doc/com.comsol.help.woptics/WaveOpticsModuleUsersGuide.pdf, accessed in 2023.

[47] Lameirinhas, R. A. M., J. P. N. Torres, A. Baptista, and M. J. M. Martins, The impact of nanoantennas on ring resonators' performance, *Optics Communications 490,* 2021.

[48] Hiremath, K. R., Coupled mode theory based modeling and analysis of circular optical microresonators, 2005.

[49] https://refractiveindex.info, visited in 2023.

[50] Marple, D. T. F., Refractive index of ZnSe, ZnTe and CdTe, *J. Appl. Phys.* ***35***, 539-542, 1964.

[51] Yupapin, P. P., Saeung, P. and Chaichuay, C., The serially coupled multiple ring resonator filters and Vernier effect, *Optica Applicata,* Vol XXXIX, No.1, January 2009.

[52] Mason, S. J., Feedback theory-further properties of signal flow graphs, *Proceedings of the IRE,* **44**(7), 920-926, 1956.

A

Add-drop Double RR: Other Models

The transmittances of the throughput and drop ports, ports 2 and 4, respectively, for the analytical models of the add-drop DRR with equal coupling coefficients, A = A_2, can be represented in Figure A.1.

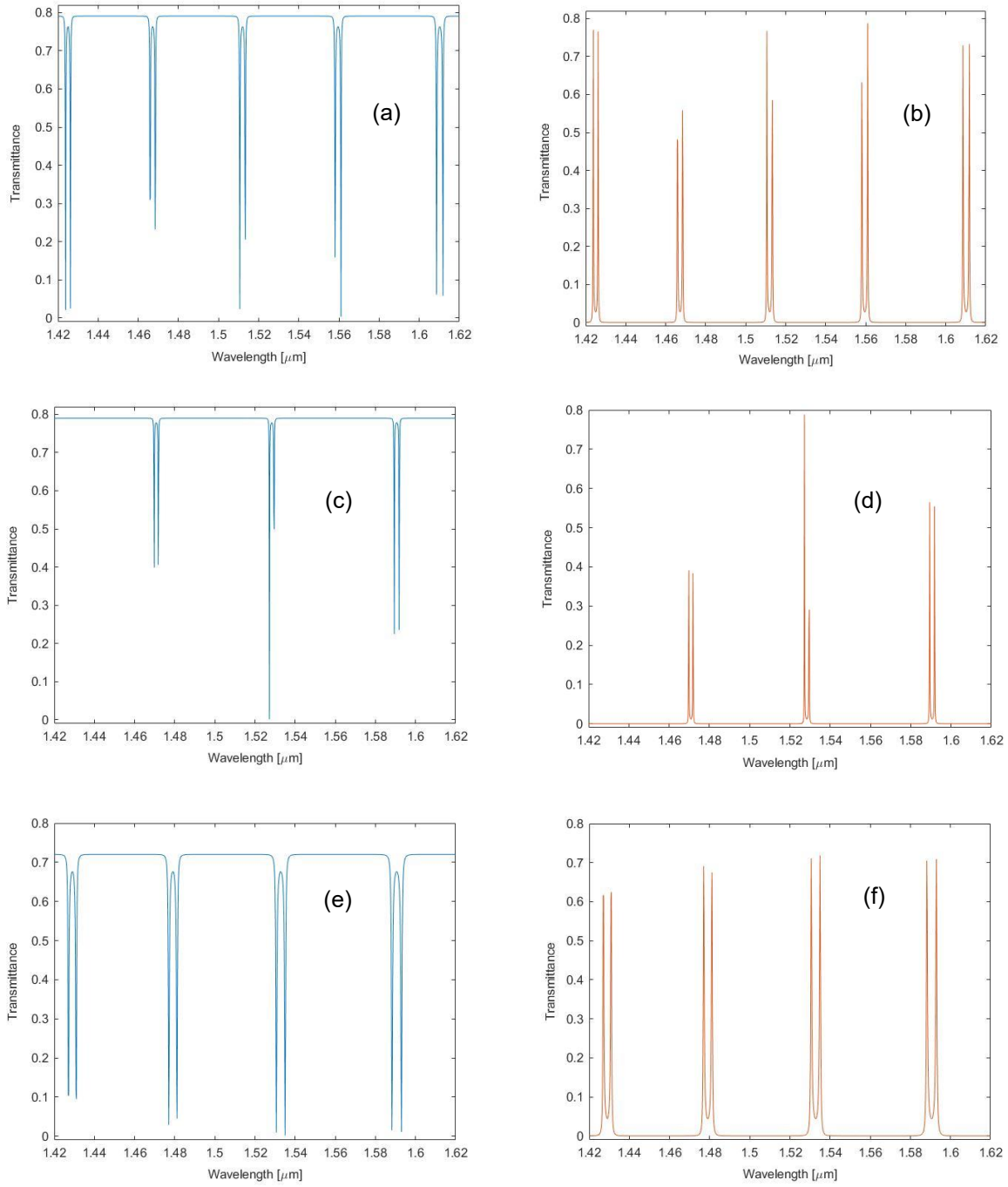

Figure A.1 – Transmittances of the analytical DRR models with A = A_2:

(a) – port 2 and (b) – port 4 : analytical DRR with a r = 2,5 μm and a n_{core} = 3,2;

(c) – port 2 and (d) – port 4 : analytical DRR with a radius of 2,0 μm;

(e) – port 2 and (f) – port 4 : analytical DRR with a n_{core} of 2,74.

For a better visualization of the similarities between the simulated and analytical results, the transmittances of the ports 2 and 4, for the add-drop double RR models, are presented in Figure A.2.

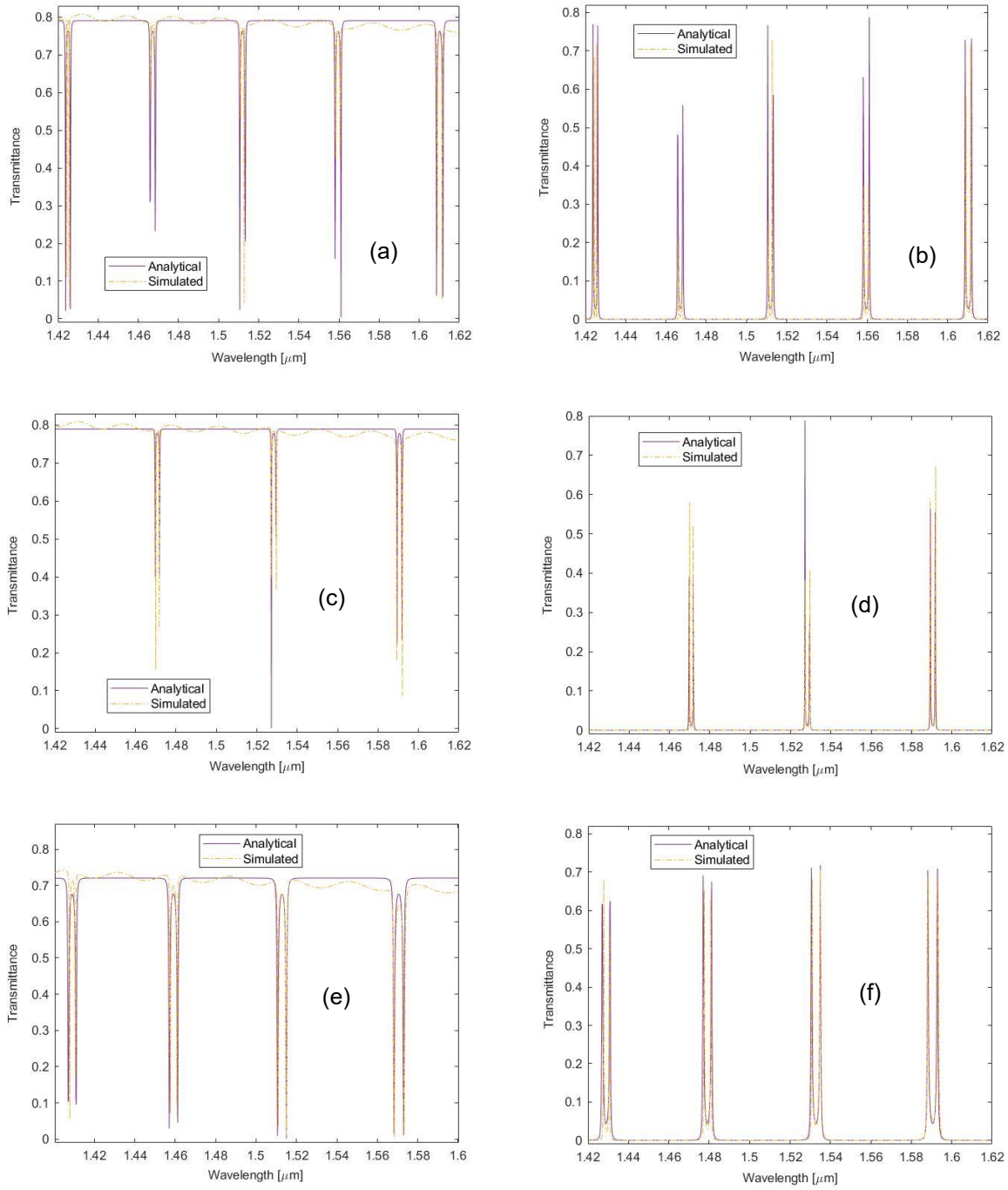

Figure A.2 – Transmittances of the add-drop DRR models, with A = A_2:

(a) – port 2 and (b) – port 4 : DRR model with a r = 2,5 μm and a n_{core} = 3,2;

(c) – port 2 and (d) – port 4 : DRR model with a radius of 2,0 μm;

(e) – port 2 and (f) – port 4 : DRR model with a n_{core} of 2,74.

Furthermore, the transmittances of the ports 2 and 4 for the add-drop DRR models with distinct radii for the 2 ring-shaped waveguides are presented in Figure A.3, being r_{left} the radius of the left ring-shaped waveguide and r_{right} the radius of the right ring-shaped waveguide considering the Figure 6.1.

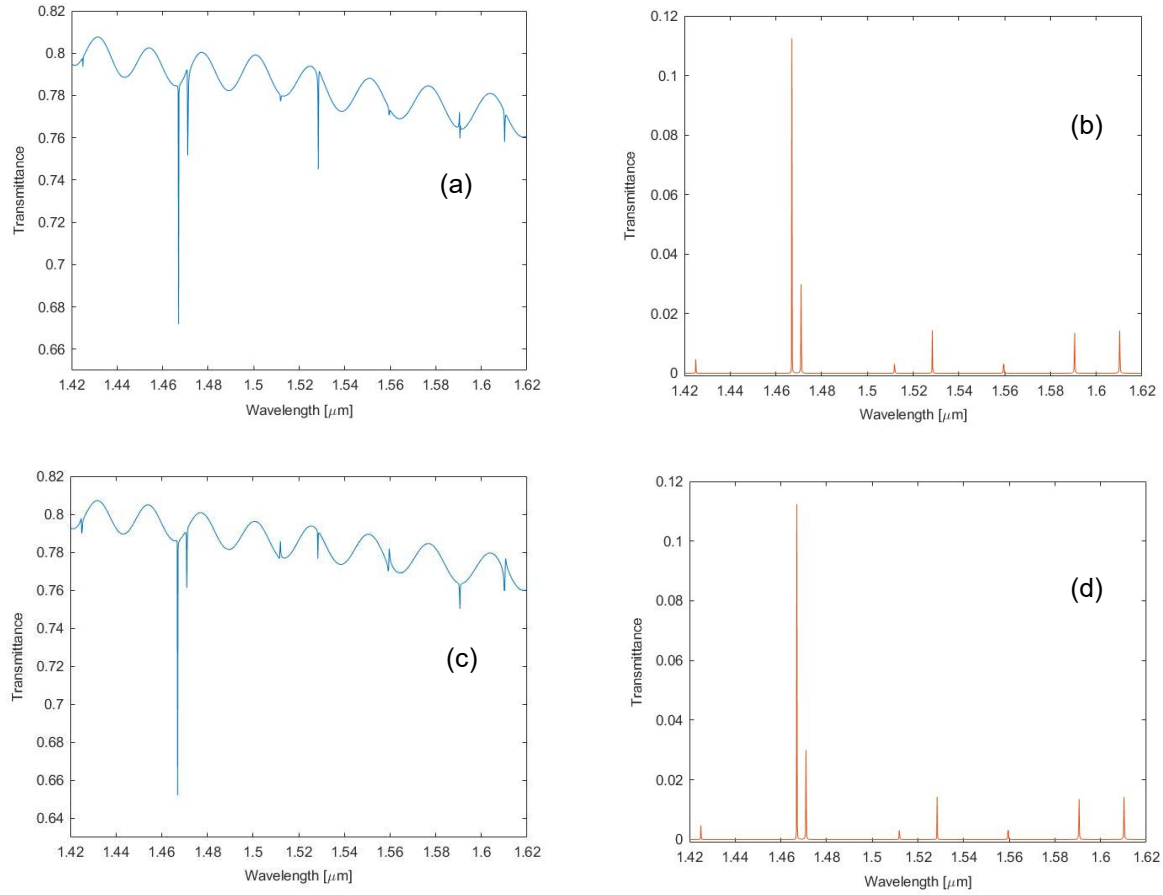

Figure A.3 – Transmittances of the add-drop DRR models:

(a) – port 2 and (b) – port 4 : DRR model with a r_{left} = 2,5 μm and a r_{right} = 2,0 μm;

(c) – port 2 and (d) – port 4 : DRR model with a r_{left} = 2,0 μm and a r_{right} = 2,5 μm.

Considering the transmittance of the DRR models presented above, the change of the radii of the ring-shaped waveguides in either side of the DRR gives similar results, with a maximum transmittance difference of around 0,03 for the port 2. Although, these models are incapable for WDM due to the lack of resonance wavelengths with a low transmittance in port 2 and a high transmittance in the drop port.

Furthermore, the analytical resonance wavelengths, of the models with equal coupling coefficients, are slightly different from the simulated ones. The maximum absolute error calculated between the resonance wavelengths obtained for both analytical and simulated models is of 0,6 nm, corresponding to 3 points difference in the parametric sweep. The error declines with the increase of the resonance wavelength for each model. The change of the transmittance values in resonance between the results from the analytical and simulated models are due to the mean values assumed for the calculus of the coefficients. This analytical DRR models can be more accurate than the models with $A \neq A_2$.

B

COMSOL Multiphysics: Model Builder

The model builder scheme used in each optical system analysed is represented by Figure B.1.

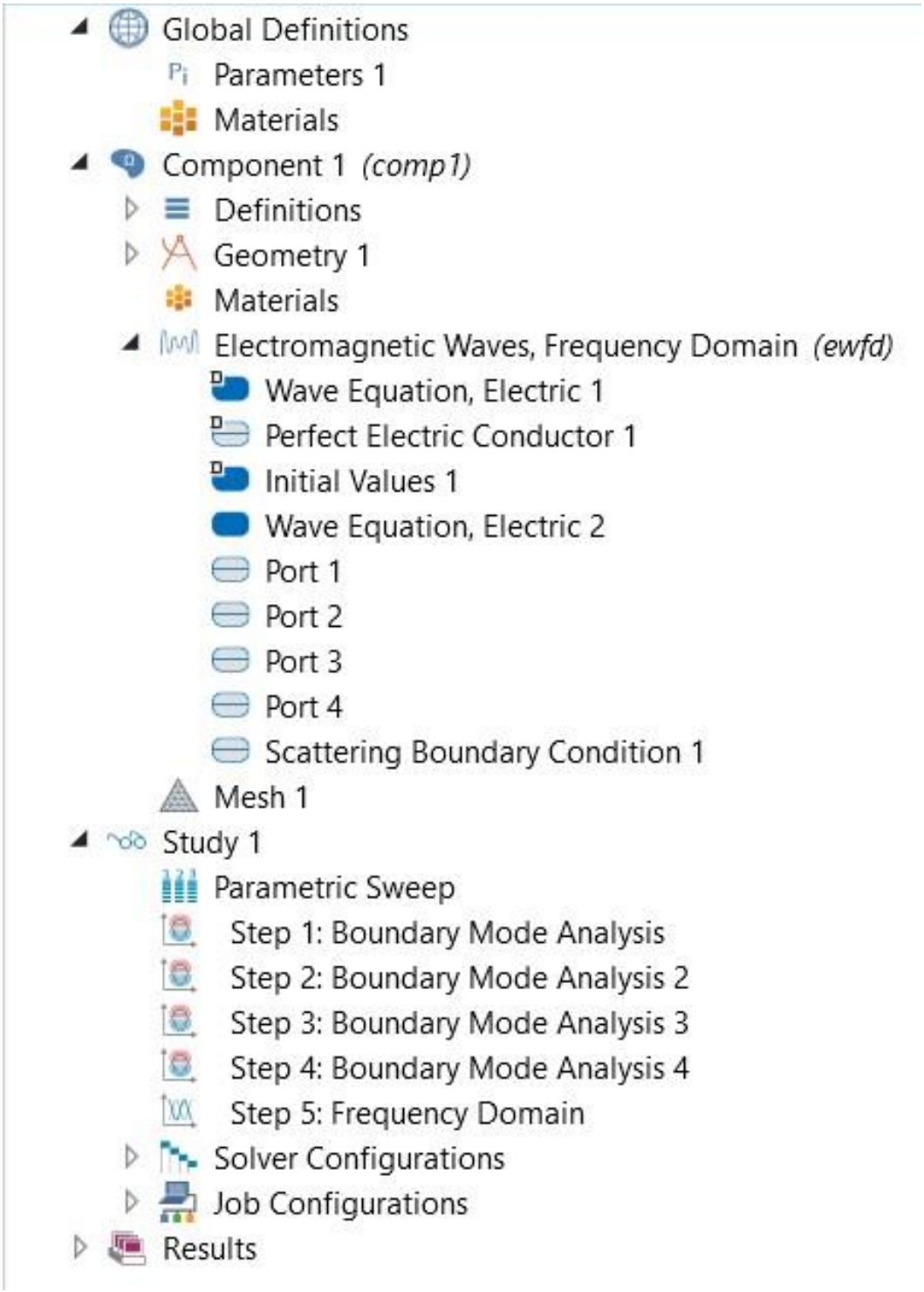

Figure B.1 – Model Builder Scheme.

C

MATLAB: Flowchart

The flowchart of the scripts used in MATLAB for the analytical method is represented by Figure C.1.

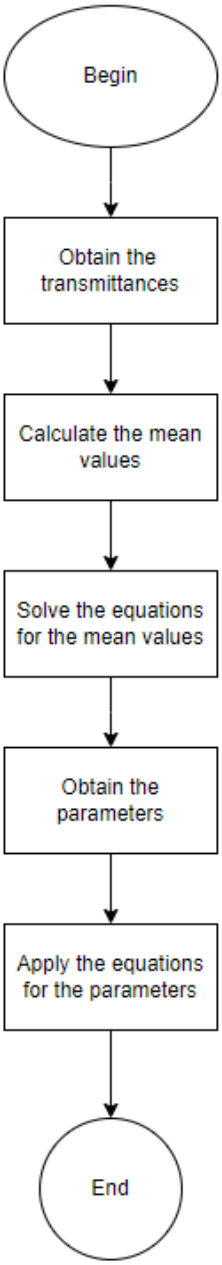

Figure C.1 – Flowchart of MATLAB scripts.